Heat flux in metal cutting

Experiment, model, and comparative analysis

Kryzhanivskyy, Vyacheslav; Bushlya, Volodymyr; Gutnichenko, Oleksandr; M'Saoubi, R.; Ståhl, Jan-Eric

Published in:
International Journal of Machine Tools and Manufacture

DOI:
10.1016/j.ijmachtools.2018.07.002

2018

Document Version:
Early version, also known as pre-print

Manuscript Draft

Title: Heat flux in metal cutting: experiment, model, and comparative analysis

Article Type: Research Paper

Keywords: Machining; Heat flux; Tool temperature; Inverse method

Corresponding Author: Dr. Vyacheslav Kryzhanivskyy, Ph.D.

Corresponding Author's Institution: Zhytomyr State Technological University

First Author: Vyacheslav Kryzhanivskyy, Ph.D.

Order of Authors: Vyacheslav Kryzhanivskyy, Ph.D.; Volodymyr Bushlya, Ph.D.; Oleksandr Gutnichenko, Ph.D.; Rachid M'Saoubi, Ph.D.; Jan-Eric Ståhl, Prof.

Abstract: In this paper, a proof of time-dependent behavior of heat flux into a cutting tool is built. Its implementation calls for a new method for estimating heat flux, which was developed using an inverse problem technique. A special experimental setup was designed and manufactured to implement the method. A series of dry machining experiments were conducted with high speed steel and cemented carbide tooling. A two-stage procedure was developed to overcome the ill-posedness of the inverse heat conduction problem by transforming it into a well-posed parameter estimation problem. The first stage retrieves the value of the heat flux and specific tool heating energy Et. The second stage parametrizes and compares predefined heat flux behaviors. It was found that the time dependency of heat flux is best described by a decreasing power function.

Heat flux in metal cutting: experiment, model, and comparative analysis

Abstract

In this paper, a proof of time-dependent behavior of heat flux into a cutting tool is built. Its implementation calls for a new method for estimating heat flux, which was developed using an inverse problem technique. A special experimental setup was designed and manufactured to implement the method. A series of dry machining experiments were conducted with high speed steel and cemented carbide tooling. A two-stage procedure was developed to overcome the ill-posedness of the inverse heat conduction problem by transforming it into a well-posed parameter estimation problem. The first stage retrieves the value of the heat flux and specific tool heating energy E_t. The second stage parametrizes and compares predefined heat flux behaviors. It was found that the time dependency of heat flux is best described by a decreasing power function.

Nomenclature

ρ – Density, (kg/m^3).
c – Specific heat, J/(kg K).
k – Thermal conductivity, W/(m K).
t – Time, s.
u – Temperature, ^{o}C.
$q, q(t)$ – Heat flux, W/mm^2.
h – Coefficient of heat exchange with the environment, W/(mm^2 K).
h_{tc} – Total thermal contact conductance, W/(mm^2 K).
n – Outward normal to boundary.
$a(t)$ – Contact length on the rake, mm.
$A = \max_{0 \le t \le T} a(t)$ - Maximum value of the contact length, mm.
TC1, …, TC8 – Acronyms of thermocouples.
b – Width of contact on the rake, mm.
m – Number of thermocouples.
$u_i^{meas}(t), u_i^{calc}(t)$ – Respective measured and calculated temperature at the position of i-th thermocouple installation, ^{o}C.
T – Modeling time, s.
t_{rot} – Time of tool engagement on the first workpiece revolution, s.
P, P_{tool} – Total amount of power consumed by the cutting process and power consumed by the tool, respectively, W.
E_t – Specific tool heating energy, J/mm^2.
β – heat partition coefficient, %.

1. Introduction

Practically all the power consumed in a cutting process is transformed into heat that is distributed between the chip, the tool body, and the workpiece [1]. For practical reasons, heat and consequently the temperature in the cutting tool are important because they determine tool wear and tool performance. The heat reaching the workpiece also influences the quality of the machined surface [2].

The temperature distribution inside the tool body is described by the classical heat equation with boundary conditions corresponding to the heat flux from the cutting zone and heat exchange with the environment [3]. However, direct measurement of these parameters in metal cutting is very difficult due to the minute contact zone for heat transfer. Temperature measurement, on the other hand, is easier, and these measurements are often used to retrieve the heat flux. This retrieval routine is known as the inverse heat conduction problem [4]. The most important feature of an inverse problem is its ill-posedness [5], primarily the fact that the solution does not exhibit continuous dependence on the initial data. As a result, small errors in the temperature measurements (initial data for the inverse heat conduction problem) can lead to unacceptable inaccuracies in

the heat flux retrieval (inverse problem solution). In particular, highly oscillatory functions, which are impossible given the physics of the process, are often returned as a solution [6].

The basic approach to overcoming ill-posedness is to use so-called *a priori* information about the potential behavior of the solution [7]. Because it is known from metal cutting practice that the heat flux does not oscillate, the solution methods are designed to exclude such cases from consideration. This procedure is called regularization and renders the problem conditionally well-posed [8].

There are three main approaches to regularizing inverse heat transfer problems: Tikhonov's regularization scheme [9], Beck's sequential function method [5] and Alifanov's iterative regularization method [4]. The main differences between them are the mechanisms used to suppress undesirable oscillations in the sought solution.

Battaglia et al. [10] proposed an approach to estimating the heat flux and the temperature at the tool tip using a single thermocouple to measure temperature at an interior point of the tool insert. A sequential function specification method and a sequential regularization method [5] were used to identify the heat flux. To avoid a non-linear heat conduction problem related to the temperature-dependent properties of materials, a model expressed in a recursive transfer function form was proposed. Lately, this approach has been extended to drilling and milling [11, 12]. In all cases, retrieved heat flux values were used for estimation of cutting tool temperature.

Two principal improvements were made by Norouzifard and Hamedi [13, 14]: temperature distribution in the tool was computed by performing transient thermal analysis in 3D, and multiple thermocouples inserted at various tool locations provided the inverse solver with input data. The inverse procedure was also based on Beck's sequential function specification method [5]. This procedure uses superposition principles and Duhamel's superposition, and therefore deals only with linear heat conduction problems.

To take into account both the nonlinearity of the heat conduction problem and the complex geometry of a cutting tool, Brito et al. [15] proposed the use of specification function techniques [5] implemented as a MATLAB program in conjunction with a COMSOL Multiphysics environment. The heat flux to the tool was based on the experimental temperature readings. This flux information was then used for reconstruction of the temperature field in a cutting tool.

C.-H. Huang et al. [16] proposed another approach to solving the inverse problem using a steepest descent method to estimate the heat flux to the tool in a drilling operation. Thermocouple readings were used to obtain the heat flux along the drill bit edge at two cutting speeds. The proposed inverse problem technique is a combination of three separate problem solutions: the direct heat conduction problem, the sensitivity problem, and the adjoint problem. In their study, the developed technique works only with temperature-independent properties of materials or linear cases.

Putz et al. [17] developed a method to determine the generated thermal energy and heat fluxes partitioned among workpiece, tool, and chip using infrared thermal imaging. Though a new method based on retrieval of heat flux from generated heat energy was proposed, it was tested only for 2D geometrical models and linear heat transfer cases.

Study of the behavior of computational heat fluxes has found that: (i) heat flux grows relatively slowly after tool engagement (approx. 10 s), (ii) practically stabilizes with small residual oscillations at a certain level or demonstrates a slow growth, and (iii) decreases over a short period of time (approximately 5 s) after tool disengagement [10, 13, 14, 15]. Other researchers [17, 18, 19] reported constant or near-constant heat flux behavior over the machining time. However, this flux behavior differs from the behavior observed during metal

cutting, where the temperature in the primary, secondary and tertiary zones reaches its maximum value almost instantly [1]. At the end of machining, the flux should fall to zero abruptly. This weak point of the methods was mentioned by Norouzifard and Hamedi [13]: “These methods deform the shape of the estimated heat flux versus time diagram especially at the regions that the heat flux changes sharply (the start and the end of machining)”. Practically all above-mentioned studies utilized heat flux information for reconstruction of temperature field in a cutting tool. In this context, potential inaccuracy of retrieved flux may lead to an incorrectness in calculated cutting tool temperature.

Earlier study by the authors [20] investigated the possibility of matching the experimental and computational data by applying a decreasing heat flux behavior. However, it was not demonstrated if such behavioral trend describes experimental data more adequately than the above-mentioned constant and increasing trends.

Therefore, in this study we present a proof of heat flux behavior over time. To achieve this, we develop conditionally well-posed inverse problem approach that retrieves both the value of heat flux into the tool, and establishes its time resolution. To implement this approach, a sensitivity analysis was carried out, two-stage procedure was developed, a special experimental setup was designed and manufactured, specially selected machining tests were performed, and a computational model was built in a COMSOL Multiphysics environment.

2. Methods

2.1. Experimental setup

As mentioned above, the inverse heat conduction problem is very sensitive to accuracy of measurement and modeling uncertainties [6]. Therefore, the following aspects were taken into account in the design stage concerning the test setup, modeling, and experimental conditions.

1. Machining operation. Orthogonal cutting experiments were performed without coolant as these conditions provide a simple and defined geometry of the tool-chip contact surface.

2. Experimental test array. The materials used in the tool and workpiece pair and the cutting conditions (Table 1) were chosen to avoid flank wear and cratering, which would be additional unknown heat sources.

3. Tool design. The cutting tools were manufactured as solid rectangular bars with a square cross section of side 25 mm and 180 mm length. The tools were ground to provide simple geometry of the cutting edge with a rake angle $\gamma = 0^{o}$, clearance angle $\alpha = 7^{o}$, and edge radius $r_{\beta} = 20$ µm. Using a solid tool made it possible to avoid the uncertainties inherent in tool assemblies related to the undefined thermal contact parameters at, for instance, the insert-clamp plate, insert-anvil, and anvil-toolholder. The manufactured solid tools corresponded to ISO PCLNL2525M25 geometrical dimensions. Initial modeling and experimental findings showed that smaller tool dimensions are subject to significant size-effects with respect to thermocouple junctions and the heating-cooling balance.

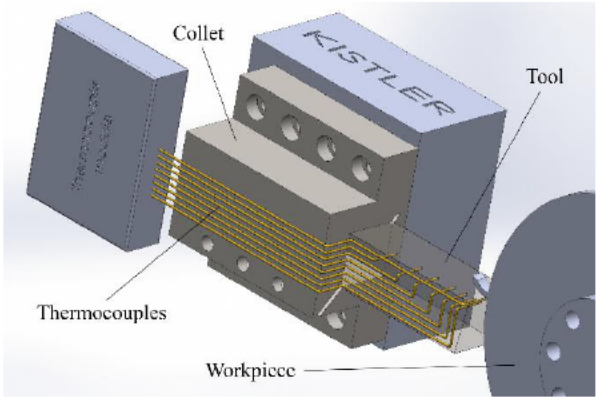

Fig. 1. Schematic of the designed experimental setup.

4. Cutting tool mounting system. A special collet (Fig. 1) was manufactured to mount the experimental tools on the lathe. It is designed to provide a fixed tool-collet contact surface to enable accurate modeling of thermal contact or thermal resistance. During the assembly, tool-collet contacting surfaces were covered with high thermal conductivity silicone paste OMEGATHERM® 201 to avoid uncertainty regarding the gas conductance parameters and to ensure reliable calculation of gap conductance (see Section 3.3.4).

5. Thermocouple installation. Previous studies [21, 22] recommended that very thin thermocouples and holes parallel to the isotherms (normal to the temperature gradients) should be used to minimize disturbance to temperature distribution and constriction resistance due to the gage. Therefore, fine-gauge Kapton insulated thermocouples (Omega Engineering) SC-KK-K-40-1M with a wire diameter of 80 μm, providing a fast response, were used to record temperature. Fine holes with a diameter of 0.5 mm and depth of 12.5 mm for the thermocouples were made using sink EDM. As a result, the positions of thermocouple junctions correspond to the center-plane of the tool. The coordinates of the appropriate holes are shown in Fig. 2. The following rationale was used to determine the positions of the thermocouples along the tool body. As reported in [22, 23], the placement of thermocouples in zones with high temperature gradients significantly increases the errors in their readings, and remote installation leads to decreased sensitivity. Therefore, the thermocouples were placed along the tool body in such a way that their readings uniformly cover the range of measured temperatures. Preliminary FE simulations have shown that the desired goal can be achieved by installing thermocouples in coordinates that correspond to Fibonacci numbers (Fig. 2).

Prior to installation the thermocouple junctions were additionally electrically insulated with amorphous SiO thin film with a thickness of 200–400 nm to avoid parasitic currents. The holes were pre-filled with high temperature air set cement OMEGABOND® OB-300 in a vacuum chamber. After thermocouple installation, the uniformity of cement media was restored by vacuum-assisted infiltration. Finally, the thermocouples were immobilized by gluing them onto the free surfaces of the tools.

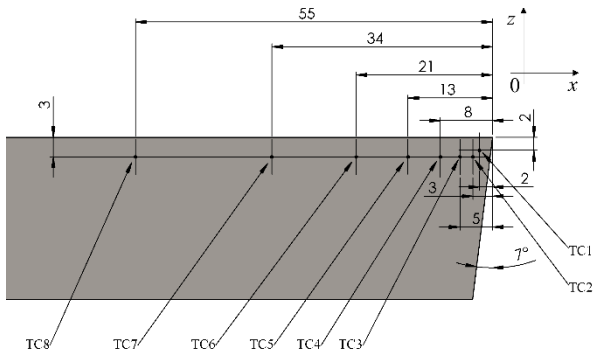

Fig. 2. Coordinates of holes for thermocouple installation.

2.2. Boundary value problem

Temperature distribution in a solid body is described as a boundary value problem for the heat equation. In this case, the heat equation is homogeneous and solely reflects the energy conservation law for any interior point in the body (Eq. 1).

$$div(k(u)grad\ u) = \rho c_p(u)\frac{\partial u}{\partial t} \tag{1}$$

To obtain the mathematical description of the temperature field in our experimental setup, the object of the modelling included both the solid tool and the collet, and adequate boundary conditions were applied on the free boundaries of the bodies and on their contacting surfaces (Fig. 3).

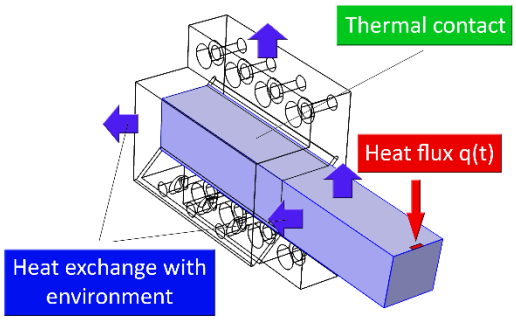

Fig. 3. Schematic of boundary conditions for the heat transfer problem.

Fig. 3 illustrates the heat flux $q(t)$ specified on the tool-chip contact surface (Eq. 2), thermal contact between the tool and the collet (Eq. 3), and the conditions of heat exchange with the environment applied on other remaining surfaces (Eq. 4).

$$k(u)\frac{\partial u}{\partial n} = q(t), \tag{2}$$

$$-k_{tool}\frac{\partial u_{tool}}{\partial n} = -h_{tc}(u_{collet} - u_{tool}), \tag{3}$$

$$-k_{collet}\frac{\partial u_{collet}}{\partial n} = -h_{tc}(u_{tool} - u_{collet}),$$
$$-k(u)\frac{\partial u}{\partial n} = h(u - u_{ext}), \quad (4)$$

The initial condition (Eq. 5) for equation (1) completes the boundary value problem statement

$$u|_{t=0} = u_0. \quad (5)$$

It is worth noting two important characteristics of this model. The first one relates to consideration of tool engagement on the first workpiece revolution. The second relates to the necessity of properly describing the thermal contact, particularly in cases of long-duration cutting processes, complicated tool assemblies, and tool materials with high thermal diffusivity.

2.3. Material properties

The first set of solid tools was manufactured from high speed steel Uddeholm 24UC [24], which was heat treated to 63 HRC (Fig. 4a). The second set of tools was made from a solid bar of fine-grained cemented carbide H10F (Fig. 4b).

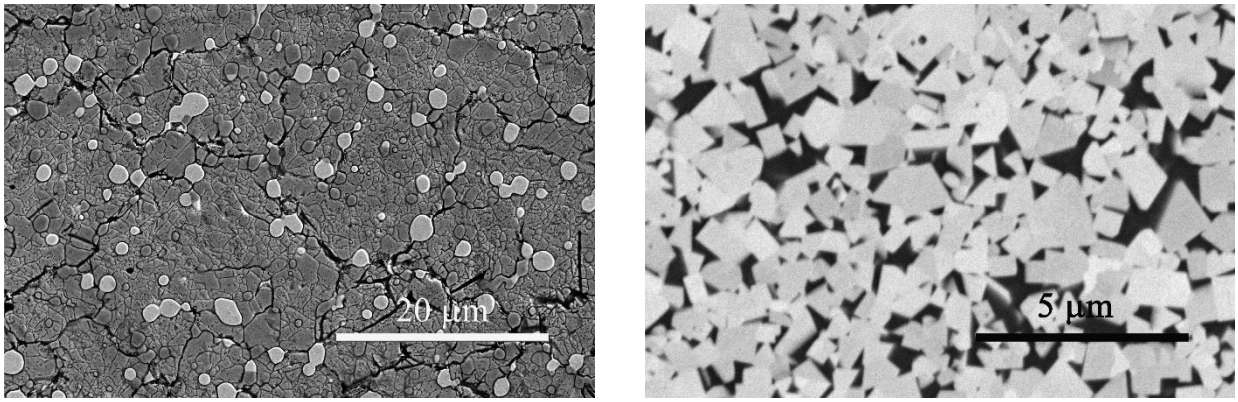

a) b)

Fig. 4. Microstructures of tools.

Because all tools were custom manufactured and heat treated specifically for these experiments, their thermal properties require refinement. The temperature-dependent thermal properties of both cutting tool materials were measured on Light Flash Apparatus LFA 467 HT HyperFlash in the temperature range RT–900 °C (Fig. 5).

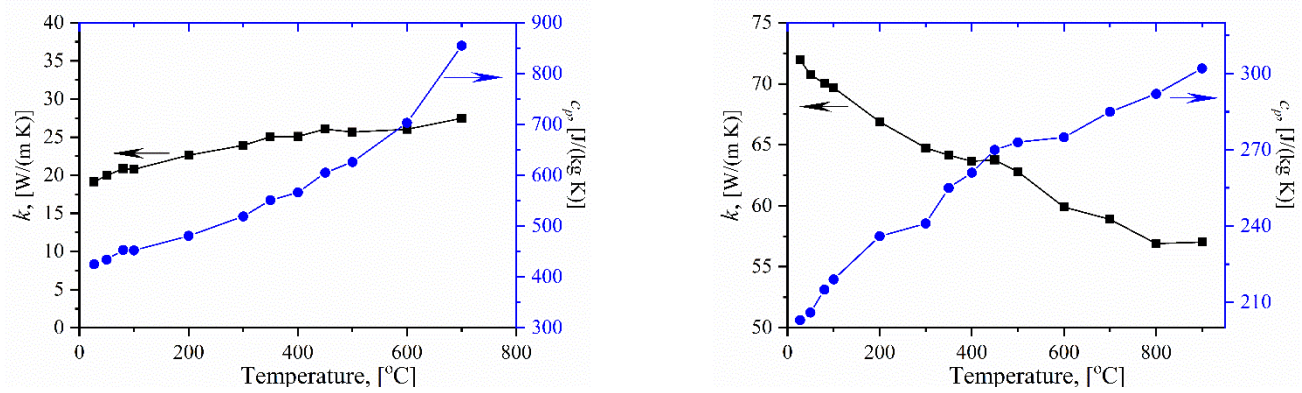

Fig. 5. Thermal properties of (a) high speed steel and (b) cemented carbide tool materials.

2.4. Experimental work

To analyze the above thermal phenomena, orthogonal cutting tests were performed on a 70-kW SMT 500 CNC lathe that was able to maintain a constant cutting speed as the diameter of the workpiece reduced during machining. The experimental setup is presented in Fig. 6. Two workpiece materials were employed: aluminum alloy 5457 and EN S235JR (1.0038) steel. Depending on the experiments, the workpiece was between 424 and 470 mm in diameter and 4 mm in thickness (Table 1). A large workpiece like this made it possible to achieve the desired prolonged tool engagement. The workpiece disks were clamped in a specially designed fixture. The mounting surfaces of the fixture were finish machined prior to each disk installation in order to minimize the radial and axial runout. This clamping provided an axial runout of 0.25 mm at maximum diameter. The disks were initially clean-cut to remove the radial runout. The experimental assembly also included a three-component Kistler dynamometer (Kistler 9129AA) to record the dynamic changes in the cutting forces. The thermocouple signals were acquired using MATLAB® data acquisition software and a National Instruments high-density thermocouple module (NI9213).

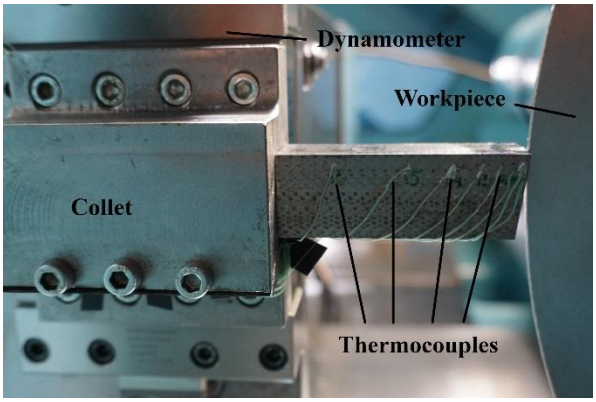

Fig. 6. Photograph of experimental setup.

As an additional precaution, chips during machining were removed from the vicinity of the cutting zone in order to avoid uncontrollable heat sources on the side surfaces of the cutting tools.

3. Results and discussion

3.1. Data

Four experiments were conducted. The parameters are shown in Table 1.

Table 1.

Experimental test array.

Experiment acronym	**Cutting conditions**		**Materials**		**Disk diameter, mm**
	Cutting speed, m/min	Feed, mm/rev	Workpiece	Tool	
HSS1	300	0.1	Aluminum 5754	High speed steel	470
HSS2	300	0.15	Aluminum 5754	High speed steel	470
CC1	100	0.05	Steel EN S235JR	Cemented Carbide	450
CC2	100	0.1	Steel EN S235JR	Cemented Carbide	424

The experimental thermocouples readings are depicted in Fig. 7.

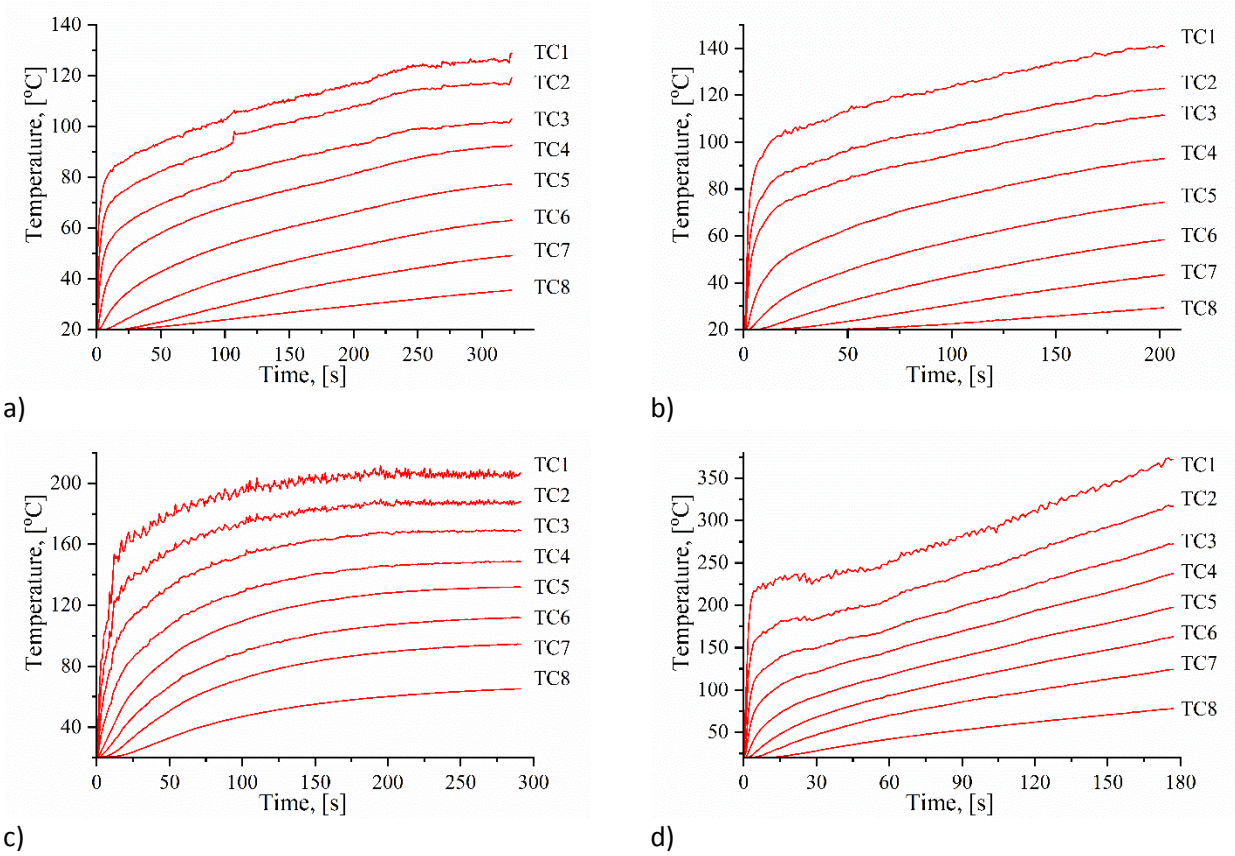

Fig. 7. Thermocouple readings for experiments: (a) HSS1, (b) HSS2, (c) CC1, and (d) CC2.

The experimental data for the cutting force component F_c are shown in Fig. 8. These data are used to estimate the total power consumed in the cutting process, defined as the product of cutting force F_c and cutting speed v_c, and also to calculate the heat partition coefficient β (shown later in Table 4).

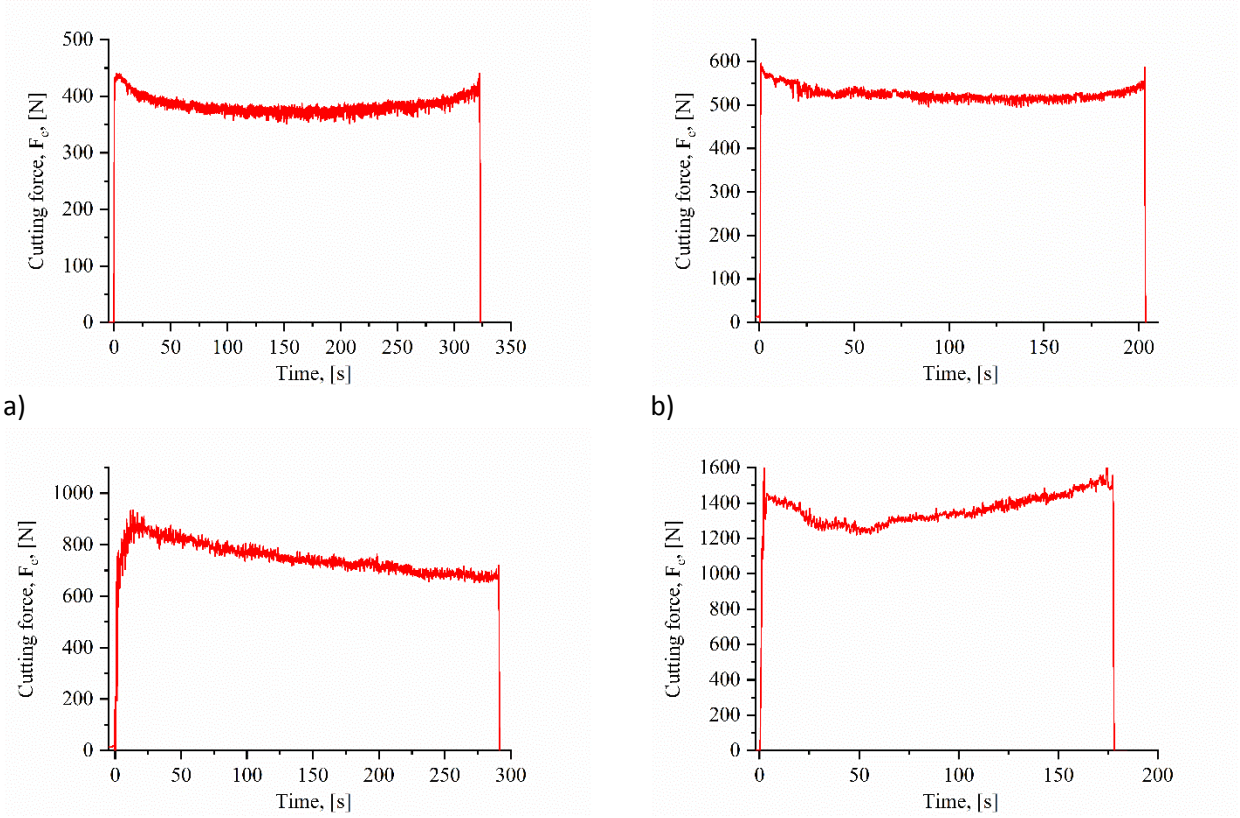

Fig. 8. Measurement of cutting force: a) HSS1, b) HSS2, c) CC1, and d) CC2.

After tool disengagement, microscopy of the tool-chip contact zone (Fig. 9) enabled observation of the maximal area of tool-chip contact interface that was active during the tests. The tools were also inspected for the presence of tool wear. An insignificant cratering of KT=11 µm was found only in CC2 case, while other cases were had no tool wear.

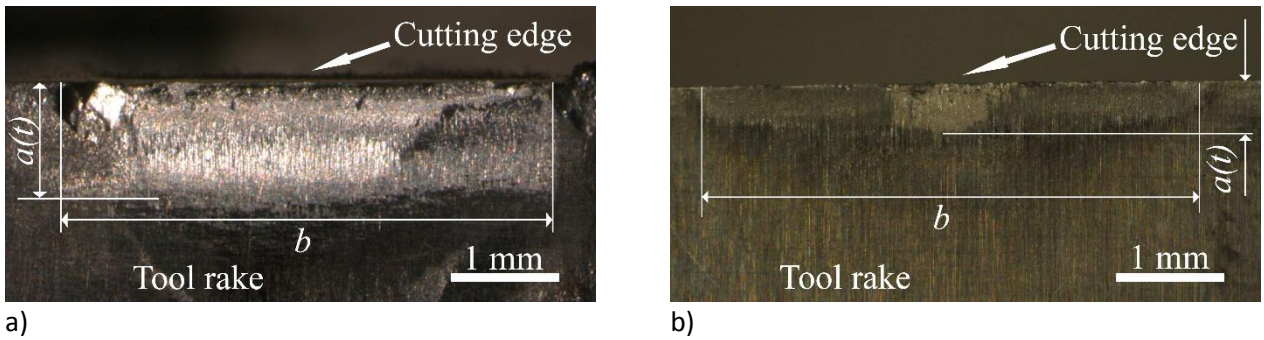

Fig. 9. Optical micrograph of the tool-chip contact area on the rake for (a) HSS2 and (b) CC1 tests.

3.2. Contact area analyses

Fig. 9 shows examples of the optical microscopy for the contact area. The dimensions of the observed area reflect only the largest width and length that occurred over the entire duration of the experiment. The observation does not represent variation of contact dimensions over the test time. For example, the axial runout of the disk reduces as the disk diameter decreases during machining. This affects the observable contact width *b*, which visually will be largest at the largest disk wobble. It was found that the contact width *b* is 20–30

% larger than the original disk width of 4.0 mm, as seen in Fig. 9. Taking the chip widening and the axial runout into account still does not completely compensate for the observed contact width *b* discrepancy.

Fig. 10 shows an image of the chip root attached to the disk obtained using a quick-stop device when machining EN S235JR steel with the cemented carbide tool. It can be seen that burr formation can also significantly contribute to the contact area width *b*, yet it does not introduce thermal load – it only distorts the visible tool-chip contact width. To avoid this misleading information, the contact width *b* was assumed to equal the chip width. The value of *b* was obtained as an average of 50 chip width measurements for each machining experiment (Table 4).

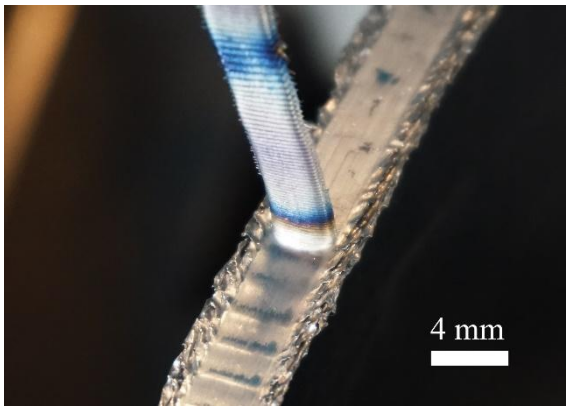

Fig. 10. Quick-stop image showing a chip attached to EN S235JR steel disk.

The same effect of contact dimension variation during machining applies to the contact length *a*. Trent and Wright [25] argue that the presence of oxide films on the tool surfaces results in frictional conditions during the engagement phase that are different from the conditions during later continual machining, when such films have been removed. Fig. 11 illustrates the variation of the cutting and feed force components in the CC1 experiment. The feed force F_f, or frictional force in our case of an orthogonal test with $\gamma = 0°$, does not follow the behavior of the cutting F_c component.

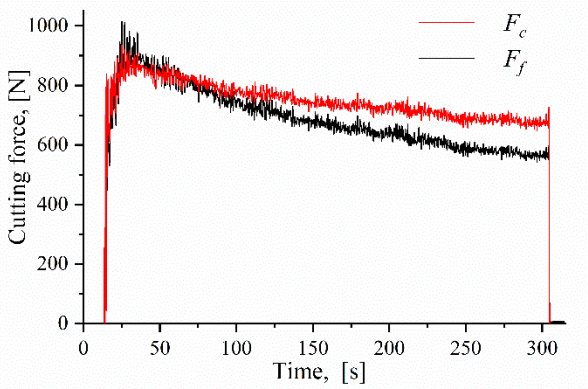

Fig. 11. Cutting F_c and feed F_f force components for the CC1 machining test.

Fig. 12 plots the ratio between the frictional or feed component and the cutting component F_f/F_c. It can be seen that the ratio F_f/F_c demonstrates (i) rapid increase during the engagement, particularly noticeable in the CC1 and CC2 tests. This stage is followed by (ii) a decreasing trend with (iii) subsequent stabilization. This illustrates that the frictional behavior on the tool-chip interface [25] indeed varies over the machining period.

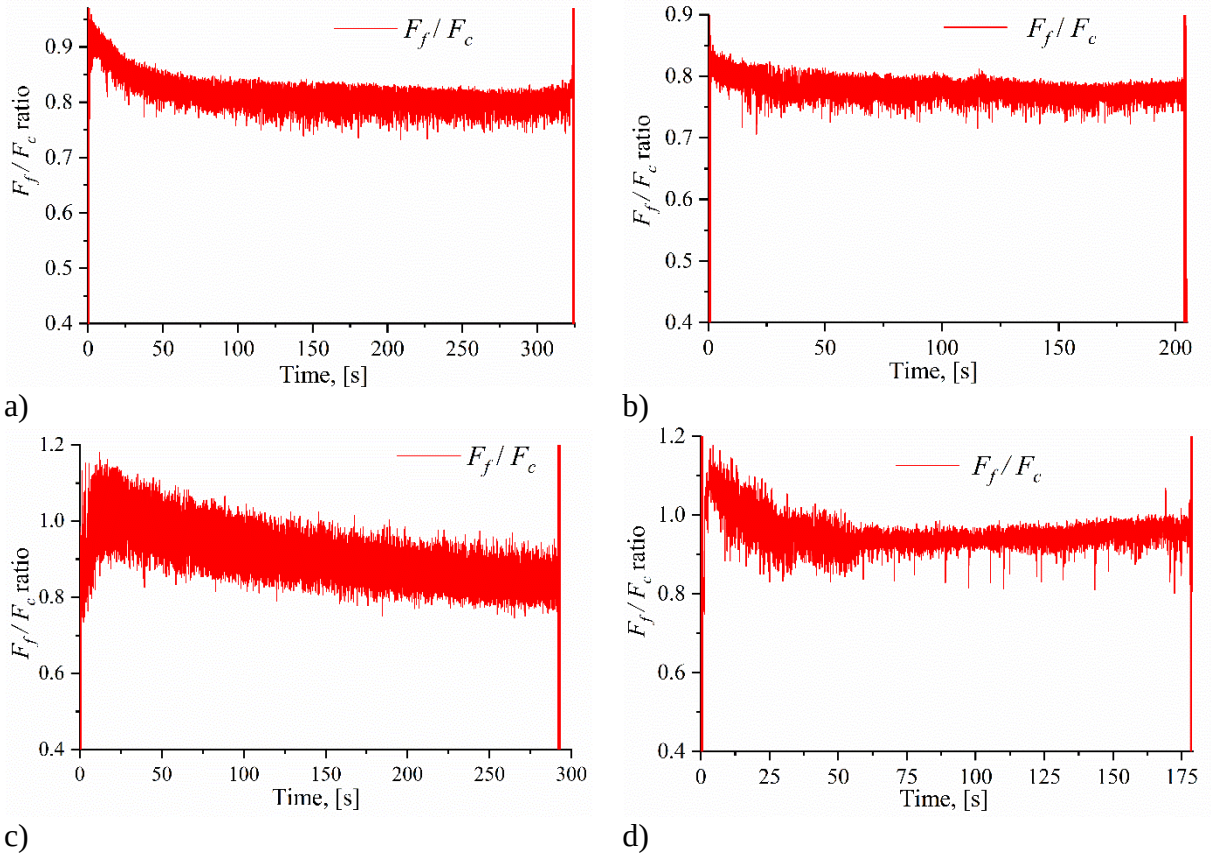

Fig. 12. Ratio of the feed F_f to the cutting F_c force components: (a) HSS1, (b) HSS2, (c) CC1, and (d) CC2.

Ostafiev et al. [26] experimentally demonstrated that not only the frictional conditions but also the contact length *a* change during the entire tool engagement process (Fig. 13a). The procedure [26] involved orthogonal turning with initial radial tool feeding, which was followed by a tool side motion via simultaneous radial and axial feeding, and concluded with radial feeding again. The same effect on the contact length *a* was observed when we followed this procedure. Initial tool engagement was accompanied by larger contact (Fig. 13b) as compared to the length at the end of machining test (Fig. 13c). Both SEM and respective *Al* and *Fe* EDX maps confirm that the contact length *a* measured in region 1 of Fig. 13a is larger (Fig. 13b and 13c) than the contact length in region 2 of Fig. 13a.

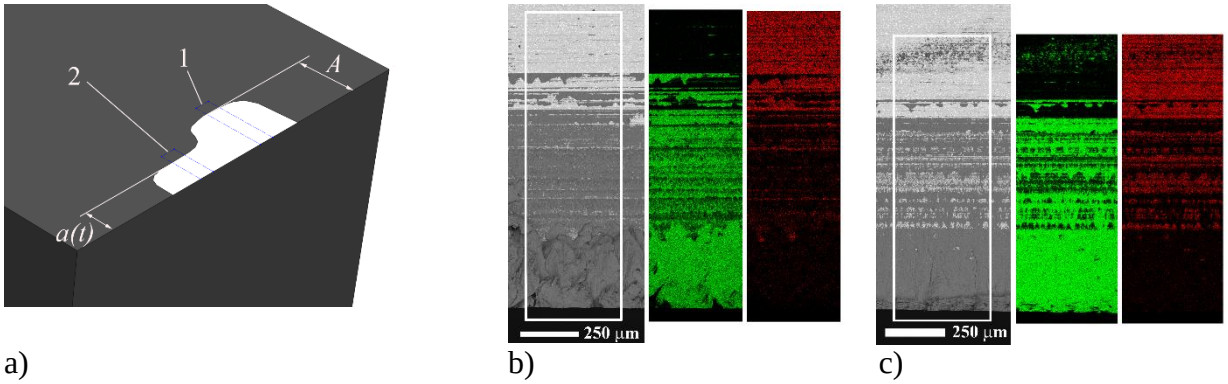

Fig. 13. (a) Schematic of the contact area on the tool rake adapted from [26]. Contact length *a* during tool engagement (b) and tool exit (c) in radial-axial cutting test HSS2.

Forces were also recorded during the radial-axial cutting tests [26]. The calculated F_f/F_c ratio similarly demonstrates the earlier observed (Fig. 12) variation of the frictional conditions. In both cases the initial peak in the force ratio is followed by a rapid decrease in the case of HSS2 (Fig. 14a), and less pronounced decrease in the case of CC2 (Fig. 14b). The findings in Fig. 13 and Fig. 14 allow the assumption of strong correlation between the contact length a and the force ratio F_f/F_c.

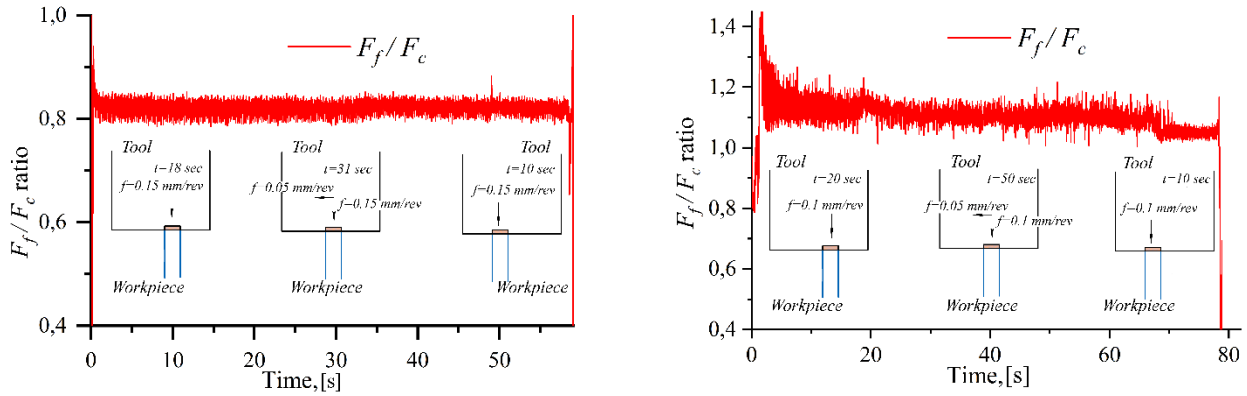

a) b)

Fig. 14. Variation of the force ratio F_f/F_c during radial-axial cutting tests which correspond to the conditions of (a) HSS2 and (b) CC2.

An additional argument, which demonstrates that the F_f/F_c ratio reflects the variation of frictional conditions, was found when performing chip formation analysis for all the experiments (Fig. 15). The chip compression ratio λ_h found for the average chip thickness h_2 calculated from the optical images of chip cross-sections (Fig. 15) is around $\lambda_h \approx 3.5$ for machining aluminum alloy 5457 and $\lambda_h \approx 5.5$ for the case of steel EN S235JR (Fig. 16).

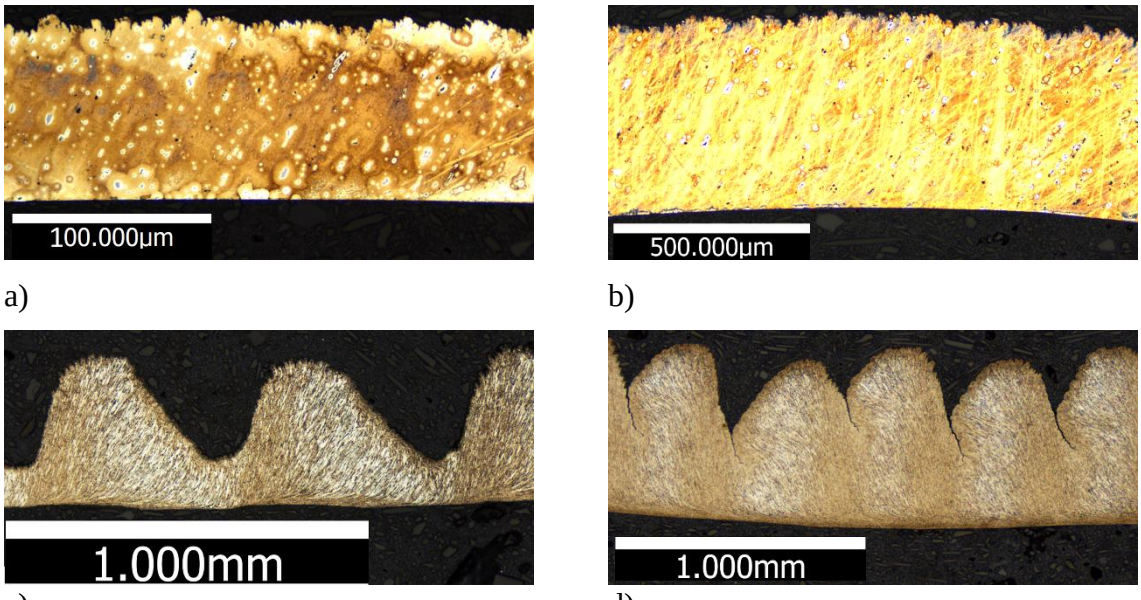

a) b)

c) d)

Fig. 15. Optical micrographs of the chip cross section for (a) HSS1, (b) HSS2, (c) CC1, and (d) CC2 cutting tests

Calculation of the shear plane angle φ [1] indicates that this angle attains values of ≈10° and ≈15° for CC and HSS tests respectively (Fig. 16). At such low angles, the force acting on the shear plane F_s [25] is dominated by the cutting force component F_c, while the feed component F_f predominantly reflects the friction on the rake

face. Thus, in our case, the F_f/F_c ratio describes the variation in rake friction and chip formation processes. Therefore, based on the observed correlation, the four phases found for the force ratio (Fig. 12) are also assumed to occur for the contact length *a(t)*, that is schematically illustrated in Fig. 17. Such variation of the contact length is the most probable mechanism that can explain a local maximum in the measured temperatures, which is especially pronounced in Fig. 7.d.

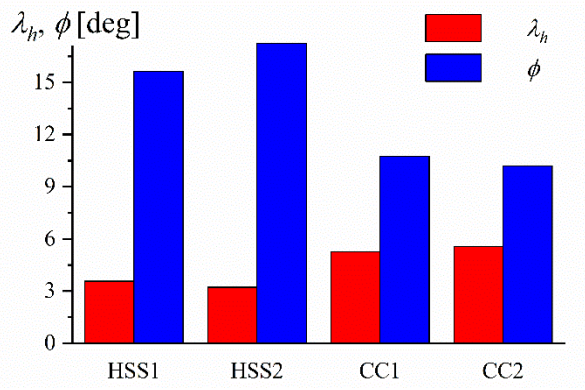

Fig. 16. Chip compression ratio λ_h and shear plane angle φ for all machining tests.

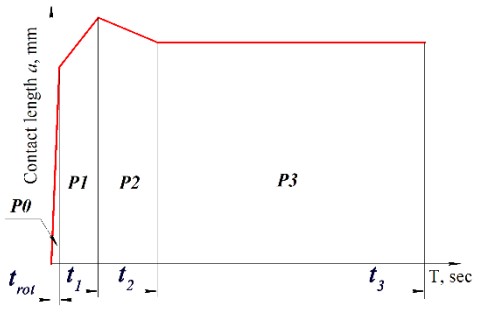

Fig. 17. Schematic of the assumed contact length *a* variation during a machining test.

The details of contact length *a* variation for each test are summarized in Table 2.

Table 2

Duration and contact length *a* for each respective phase.

Experiment acronym	Phase 0		Phase 1		Phase 2		Phase 3	
	t_{rot}, s	a_0, mm	t_1, s	a_1, mm	t_2, s	a_2, mm	t_3, s	a_3, mm
HSS1	0.3	0.74	2.3	0.86	52.3	0.81	323	0.81
HSS2	0.3	0.93	0.8	1.03	31.3	0.97	202	0.97
CC1	0.8	0.30	2.8	0.34	20.8	0.47	291	0.40
CC2	0.8	0.70	2.8	1.00	27.8	0.85	177	0.85

3.3. Computational model sensitivity analysis

Despite its simplicity, the computational model (Section 2.2) has two types of potential uncertainties. The first relates to geometric uncertainties. A thermocouple junction has physical dimensions and therefore thermocouple readings reflect an average temperature registered within the junction volume. In addition, the

exact location of the junction in the tool hole is not controllable during installation. Thus there is an uncertainty in specifying which mathematical point in the computational model is to be the thermocouple location. The term ”control points” is used to refer to those mathematical points in the model throughout the article. For the purpose of sensitivity analysis, control points for the respective thermocouples are labeled as TC1, …, TC8. The second type of uncertainty relates to the thermal characteristics of the model, such as the heat transfer coefficient to the environment h, thermal contact parameters between the collet and the tool, and the spatial distribution of the heat flux over the tool-chip interface.

The sensitivity analysis strategy consists of the formation of a realistic test case as a reference. This is followed by estimating how the two identified types of uncertainties affect the computed temperatures. To achieve the realistic case, true tool geometry was used, material properties of cemented carbide (Fig. 5b) were selected, and the tool-chip interface was taken from actual machining (Fig. 17 and Table 2). The value of heat flux q = 44 W/mm^2 was obtained with the help of the approach described in [27]. This value ensured the modeled temperatures range was close to the measured values.

3.3.1. Influence of thermocouple junction

The thermocouple junction (Fig. 18a) is a semi-sphere with a diameter of 0.2 mm. In this case the temperature registered is an average within the junction volume. Such an averaged temperature might significantly deviate from the data at the control point, especially in zones with high temperature gradients.

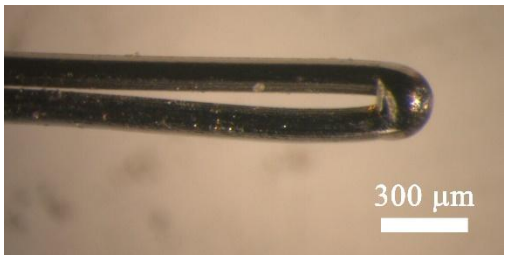

a)

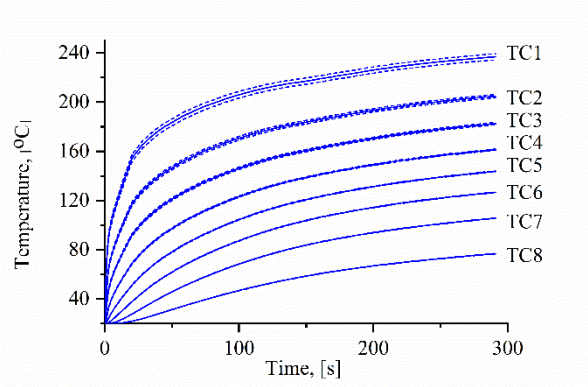

b)

Fig. 18. (a) Optical micrograph of actual thermocouple junction, and (b) influence of its size on the modeled temperature in control points.

To estimate the potential deviation, the temperature calculations were performed for control points that were shifted from the predefined positions (Fig. 2) by 0.1 mm in two directions along the axes $0z$ and $0x$ (Fig. 2). The maximum deviations are shown in Fig. 18b. In the TC1 location of the first thermocouple, the error in the temperature reading can reach 5–6 degrees. For the second thermocouple (TC2), the error is 2–3 degrees. For the other thermocouples, the error becomes negligible, that is, less than the thermocouple tolerance [28].

3.3.2. Influence of hole dimensions

The position of the thermocouple junction location in deep sinking EDMed holes (Ø 0.5 mm) relative to the axes of the holes was not controlled during installation (Fig. 19a). Therefore, to estimate the potential errors of control point positioning in the computational model, the points were shifted along the axes $0x$ and $0z$ (Fig. 2) within the radius of the hole by 0.25 mm. The largest deviations are shown in Fig. 19b. For the control points

TC1 and TC2 located in high gradient zones, the deviations reach 12 and 6 degrees respectively. From TC3 onward, the effect of the hole diameter quickly attenuates and becomes less than the thermocouple tolerance.

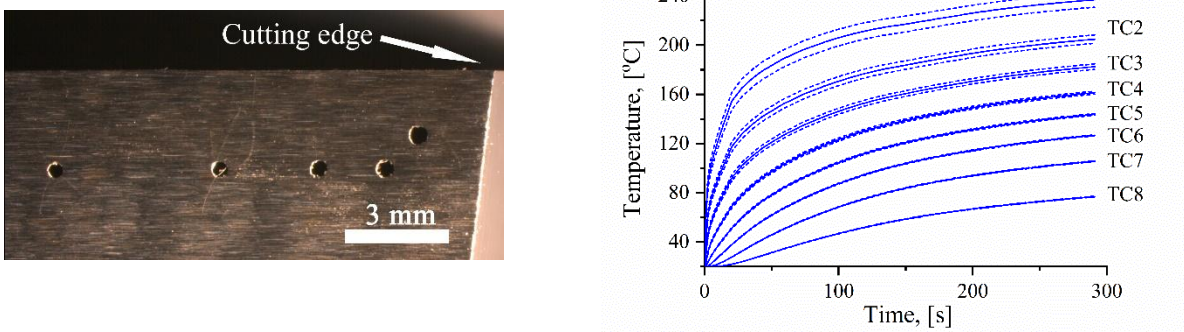

a) b)

Fig. 19. (a) Side view of the cutting tool with EDMed holes, and (b) influence of the hole size on the modeled temperature at the control points.

Both geometric analyses (section 3.3.1 and 3.3.2) indicate that uncertainty in the selection of control point positions corresponding to thermocouples TC1 and TC2 may introduce unacceptable errors. Therefore, TC1 and TC2 readings were ignored and only TC3–TC8 were considered in further modeling.

3.3.3. Influence of heat transfer coefficient to the environment, h

The coefficient of heat transfer h in (Eq. 4) characterizes the intensity of the convective heat transfer between the free tool surfaces and the environment. As shown in [14, 15], the magnitude of the heat transfer coefficient for free air convection ranges from 10 to 25 W/(m^{2}K). The computed temperatures for the sensitivity reference model at h = 5, 15, and 25 are shown in Fig. 20.

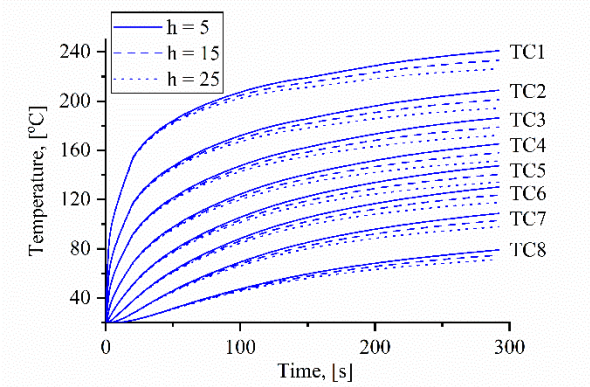

Fig. 20. Temperatures calculated for different values of h.

Fig. 20 shows that the effect of the heat transfer coefficient h on the temperatures under the cutting conditions considered is significant for all control point readings, and it should be further refined for the computational model.

3.3.4. Influence of thermal contact

In the experimental setup, a specially designed collet provides a simple and easy to model thermal contact geometry. It is known [29] that thermal contact conductance parameter h_{tc} (Eq. 3) is the sum of the

coefficients for h_c (solid-to-solid conductance) and h_g (gap conductance). While h_c can be determined on the basis of contact pressure, micro hardness, asperity average height and slope, determination of h_g requires the thermal conductivity of the medium filling the gap and, in the case of gas, the gas parameter [29]. In order to avoid these uncertainties, a thermal paste OMEGATHERM® 201 with thermal conductivity 2.3 W/(mK) was applied to the contacting surfaces. Fig. 21 illustrates the difference in the temperature modeling for two cases, one with the gap filled with thermal paste (ThCont1) and the other with the gap filled by air with typical characteristics [29] (ThCont2). Fig. 21 shows that an adequate thermal contact simulation is necessary for these cutting conditions.

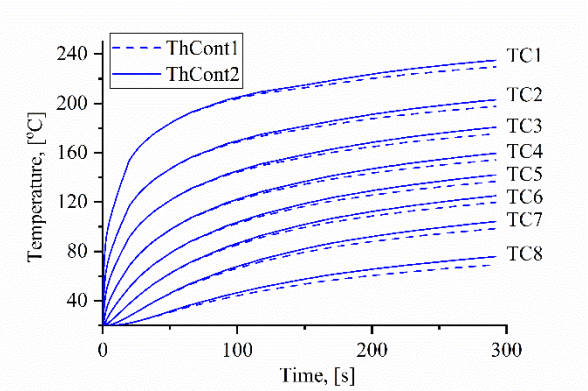

Fig. 21. The influence of thermal contact parameters on temperatures in the control points.

3.3.5. Spatial distribution of the heat flux over tool-chip interface.

The aim of this sensitivity analysis section is to estimate the influence of spatial distribution of the heat flux over tool-chip interface in the reference model. In the previous calculations, the heat flux was distributed uniformly over the tool-chip interface. This made it possible to calculate the total amount of power consumed by the tool as:

$$P_{ool} = q * Area\_of\_contact = q \int_0^T ba(t)dt. \quad (6)$$

The following test cases were formulated to investigate the effect of the spatial distribution of the flux. In the first test case, the exponential heat flux distribution [15] over the tool-chip contact region was taken as:

$$q(x,y) = C \exp\left(-\left(\frac{x-x_0}{a(t)}\right)^2 - \left(\frac{y-y_0}{b}\right)^2\right), \quad (7)$$

where C denotes the maximum value of heat flux over the tool-chip interface, and x_0, y_0 correspond to the center point of the tool-chip interface.

The second test case involves an inverse to the spatial distribution of Eq. 7 (Fig. 22a). This unrealistic test case was intentionally chosen as an extreme for sensitivity diagnostics. The third test case involves uniform spatial distribution. In all three test cases, the total amount of power P_{tool} is kept constant.

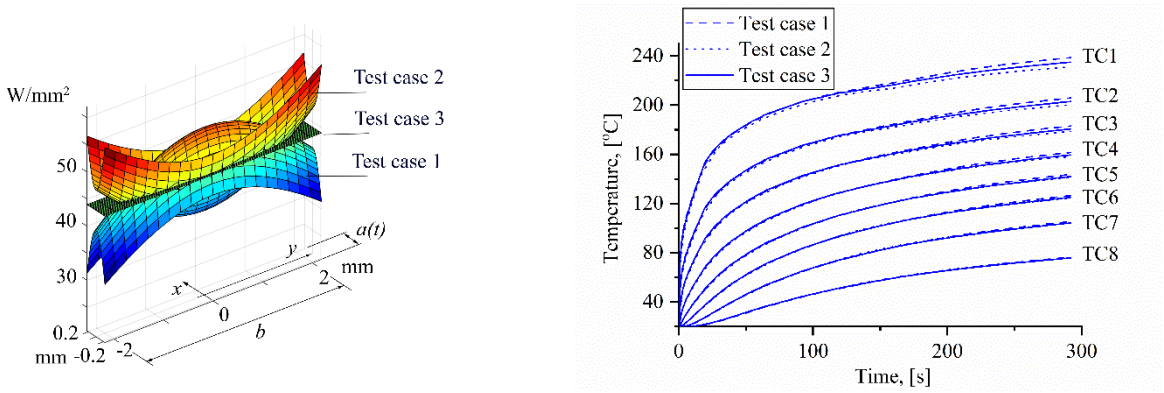

a) b)

Fig. 22. (a) Spatial distribution cases of the heat flux over the tool-chip interface, and (b) their influence on temperature calculations at the control points.

Calculations for the sensitivity reference model indicate (Fig. 22b) that the influence of the spatial distribution of the heat flux is negligible for thermocouples TC3–TC8, and therefore uniform spatial distribution can be applied in further calculations.

3.3.6. Influence of EDM hole damage.

During the electro-discharge machining (EDM) process formation of a thin oxide layer, represented by WO_3 in case of cemented carbide, is commonly observed. Tungsten oxide has significantly lower thermal properties [30, 31] than the bulk of cemented carbide, and therefore can act as a thermal barrier and may introduce potential computational errors, if ignored. Fig. 23 shows SEM image of the cross-section of an EDMed hole in the cemented carbide tool. Close-up view (Fig 23b) demonstrates that the oxide layer is not clearly visible (below 1 µm), but a recast layer, also common for EDM process, is present. Thickness of the recast layer is 10-20 µm. The chemical composition of the layer is identical to the bulk cemented carbide, yet it has much finer microstructure and a significant amount of porosity.

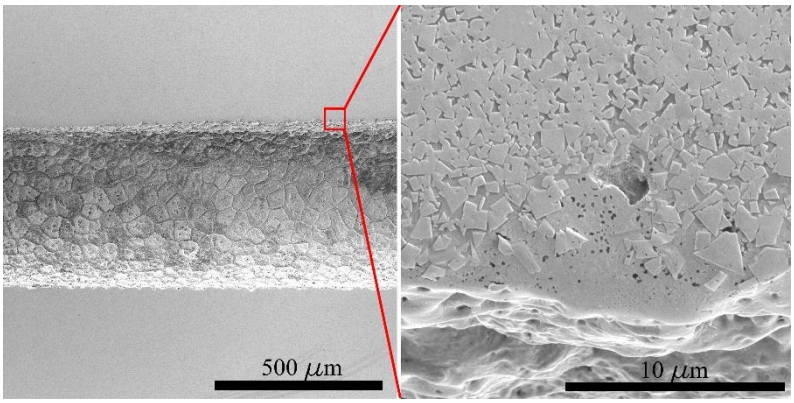

a) b)

Fig. 23. (a) SEM image of the EDM hole cross-section, and (b) close-up view of the oxide and recast layers.

Because the thermal properties of the recast layer are unknown, but expectedly lower than for the bulk, a worst-case scenario was considered where the properties of WO_3 [30, 31] were assigned to the oxide and

recast layers together. Computational model representing a solid tool was compared with a model of a tool having the 0.5 mm holes. Fig. 24a illustrates the model of a hole having the oxide and recast layer of 50 µm thickness and filled with thermal cement with defined thermal properties [32].

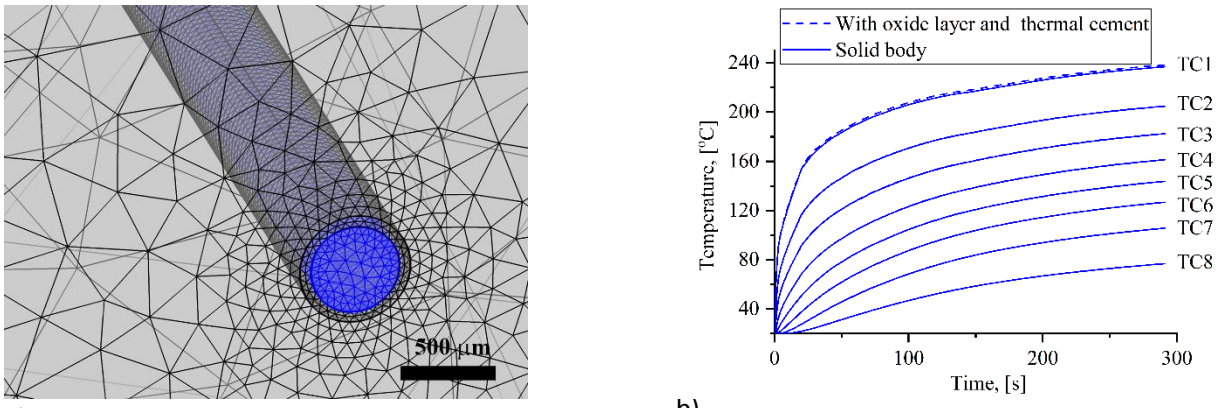

a) b)

Fig. 24. (a) Close-up view of a hole FE model, and (b) influence of EDM damage and thermal cement on temperatures in the control points.

The sensitivity analysis for the reference model, given in Fig. 24b, indicates that under worst-case conditions only the first thermocouple TC1 is affected, where the temperature error can reach up to 2 degrees. However, this potential uncertainty is below the effects of geometric factors and therefore this source of uncertainty can be left out of consideration.

3.4. Objective function

The quality of the problem solution is estimated by the convergence of the measured and calculated temperatures. Because the temperatures are functions of time, in the language of functional analysis [33] it is necessary to minimize the distance between two points in a functional space. In other words, it is necessary to create a metric in a functional space that corresponds to the problem considered. The requirements for the metric can be formulated as follows. First, because the measurement data inevitably has oscillations and the test duration of different experiments is not identical, the metric should average the oscillations over the test time and over the thermocouple readings. Second, the dimension of the metric must have a clear physical interpretation.

The metric of the space L^2 [33] corresponds to these requirements. Elements of the functional space are functions of the thermocouple readings $g^{calc}(t) = \sum_{i=1}^{m} u_i^{calc}(t)$ and functions of the measured temperatures $g^{meas}(t) = \sum_{i=1}^{m} u_i^{meas}(t)$.

The distance between these functions in L^2 metric has the form:

$$\left\|g^{calc}(t) - g^{meas}(t)\right\| = \frac{1}{\sqrt{T}}\sqrt{\int_0^T (g^{calc}(t) - g^{meas}(t))^2 dt} = \frac{1}{\sqrt{T}}\sqrt{\int_0^T \left(\sum_{i=1}^{m} u_i^{calc}(t) - \sum_{i=1}^{m} u_i^{meas}(t)\right)^2 dt}$$

$$= \frac{1}{\sqrt{T}}\sqrt{\int_0^T \left(\sum_{i=1}^{m} u_i^{calc}(t) - u_i^{meas}(t)\right)^2 dt}$$

The factor $\frac{}{\sqrt{T}}$, which is absent in the classical definition of the metric in L^2, is needed to obtain the dimension of the metric in degrees.

This allows formulation of an optimization problem in which the time dependency of the heat flux is an unknown functional variable. The objective function based on the above metric estimates the correctness of the solution by calculating the difference between the measured and simulated temperatures. This is an ill-posed function estimation problem [6]. To avoid ill-posedness, the function estimation problem was reformulated to become a parameter estimation problem, which is well-posed [6]. The reformulation is possible if the functional form of the heat flux over time is known. Thus, a limited number of parameters of this function become the variables of the well-posed parameter estimation problem, allowing us to put forward hypotheses about the functional form of the heat flux time dependency.

3.5. Three hypotheses about the time dependency of heat flux

The behavior of the heat flux found in [12, 13, 15] with the help of a sequential function specification method and a sequential regularization method [5] can be approximated by the function shown in Fig. 25a (green line). This is the first hypothesis of flux behavior over time. But in the studies devoted to spatial distribution of heat flux [17, 18] and in [19], the flux was considered to be constant over time. This is the second hypothesis shown in Fig. 25a (red line). To formulate the third hypothesis, let us consider the following. It is well known [25] that the chip reaches its maximum temperature almost instantly upon tool engagement and that the temperature remains practically constant during cutting. In terms of boundary conditions, this corresponds to Dirichlet's boundary condition [34]. This condition enforces the characteristic behavior of the flux. Maximum intensity of the flux occurs at first contact when the practically cool tool meets the chip temperature at the interface, because flux is proportional to the temperature difference. As the tool is heated up, the heat flux drops rapidly at first, and then decreases at a slower rate. This theoretical reasoning allows the assumption of a heat flux decreasing with time. However, the numerical characteristics are unknown as yet.

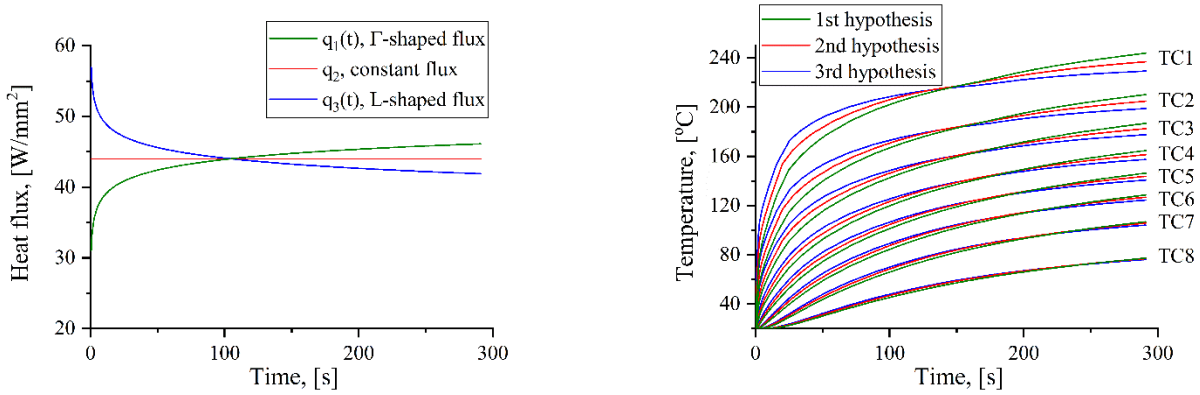

a) b)

Fig. 25. (a) Three identified flux behaviors over process time: increasing q_1 [13, 15], constant q_2 [17, 18], decreasing q_3 (this study); (b) Calculated temperature at the control points for each of the three hypotheses.

For the sake of convenience, these three hypotheses will be referred to as Γ-shaped (q_1), constant (q_2), and L-shaped (q_3) heat fluxes. As an approximation of the L-shaped time dependency, a power function with two parameters *B* and *p* can be used:

$$q(t) = Bt^p, p < 0. \tag{8}$$

However, the direct use of this curve leads to a non-integrable singularity in the boundary value problem (Eq.1 – Eq.4) solution. Therefore, the following piecewise curve (Eq. 9) is used (Fig. 26):

$$q(t, x\ , x_2) = \begin{cases} Bt_{rot}^p, 0 \le t < t_{rot} \\ Bt^p, t_{rot} \le t \le T \end{cases}, \tag{9}$$

where $p = \frac{ln(x_1/x_2)}{ln\left(\frac{t_{rot}}{T}\right)}, B = \frac{x_1}{t_{rot}^p}$.

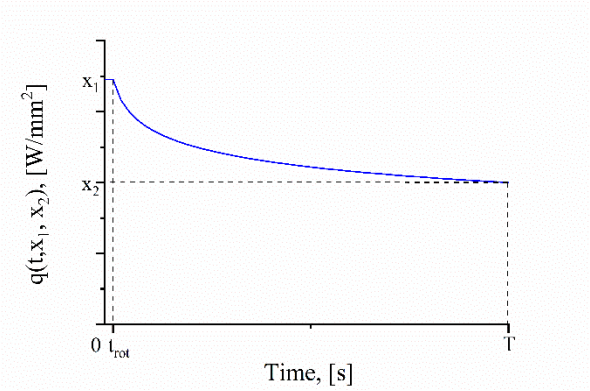

Fig. 26. The parametrized piecewise curve describing the characteristic behavior of the heat flux.

The direct use of parameters B and p in the optimization algorithm leads to its slow convergence. This is related to the difference in the magnitude of the power p and multiplication factor B, leading to an imbalance in the step increments on iterations of the algorithm. Therefore, B and p are expressed in terms of the variables x_1 and x_2 having similar magnitude.

To compare the three hypotheses, the specific tool heating energy E_t (Joules per mm^2) consumed by the tool body must be the same. Therefore, the parameters of the curves are chosen in such a way that the time integrals for all three are identical (Eq. 10):

$$E_t = q_2 T = \int_0^T q\ (t)dt = \int_0^T q_3(t)dt. \tag{10}$$

This means that the specific tool heating energy E_t is kept constant. The reference computational model (section 3.3) calculated for these hypotheses has shown that the temperatures in the remote control points (TC5–TC8) have very close values (Fig. 25b). This indicates that a constant flux is able to effectively estimate the total amount of energy needed to heat up the tool to reach the measured temperatures. On the other hand, the temperatures at the TC1–TC4 points clearly distinguish the three hypotheses. In our case the constant flux (q_2) was selected as a reference (Fig. 25b, red lines). This reference enables separation between the L-shaped flux (hypothesis 1) and the Γ-shaped one (hypothesis 3) based on the measured temperatures.

As a measure of this distinction, it is convenient to use the signed residuals between the temperatures for the L-shaped flux and constant flux for each control point (Fig. 27a). Fig. 27b illustrates the residuals between the temperatures for Γ-shaped and constant fluxes.

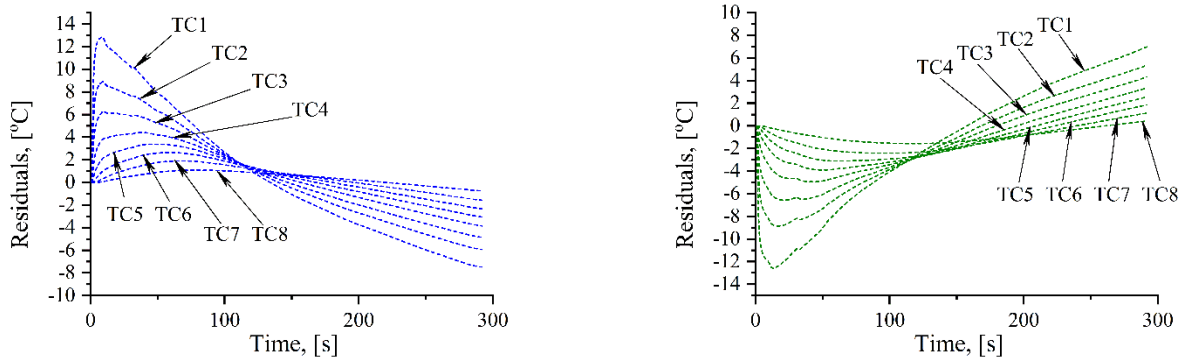

Fig. 27. Residuals at the control points: (a) for L-shaped and constant fluxes, and (b) for Γ-shaped and constant fluxes.

Comparing Fig. 27a and Fig. 27b visualizes the measure for evaluating the hypotheses. First, the constant flux has to be determined in such a way as to minimize the differences between the measured and modeled temperatures. Then the residuals between the measured temperatures and computed temperatures for this choice of constant flux are calculated. If the behavior of the residuals corresponds to Fig. 27a, then this supports hypothesis 1; if they accord with Fig. 27b, then hypothesis 3 is validated. In all other cases, neither of the hypotheses is clearly defined. Therefore a two-stage procedure for hypothesis verification can be proposed.

3.6. Two-stage procedure for hypotheses verification

3.6.1. First stage

In the first stage, the heat conduction inverse problem is solved, for which the flux is assumed to be constant over time. As mentioned, the inverse problem was reformulated from the function estimation problem to a parameter estimation problem so that it is well-posed. The mathematical representation of parameter estimation problem is as follows (Eq. 11):

$$f(q) = \left\| g^{calc}(q,t) - g^{meas}(t) \right\| = \frac{1}{\sqrt{T}} \sqrt{\int_0^T \left(\sum_{i=1}^{n} u_i^{calc}(q,t) - u_i^{meas}(t) \right)^2 dt} \rightarrow min, \tag{11}$$

subject to $0 \le q \le \frac{P}{bA}$.

In fact, this is a one-dimensional optimization problem, which can be iteratively solved, for instance, by the golden section method [35].

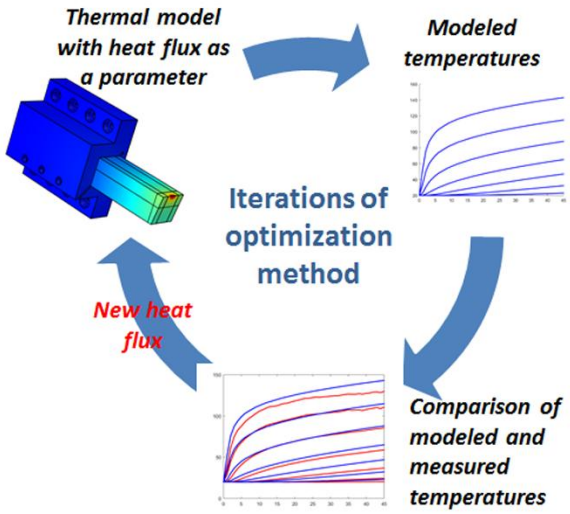

Fig. 28. The graphical interpretation of the proposed iterative method of optimization.

Fig. 28 shows the graphical interpretation of the iterative method of the mathematical programming problem (Eq. 11) solution for our case. In order to implement this method, the COMSOL model was transformed into a MATLAB function with a heat flux q assigned as a variable. This function creates a COMSOL model class in MATLAB workspace, establishes LiveLink to the COMSOL server, and sets appropriate model attribute values. When the solution converges, the calculated temperatures at the thermocouple locations are imported into MATLAB workspace where they are compared to the measured temperatures.

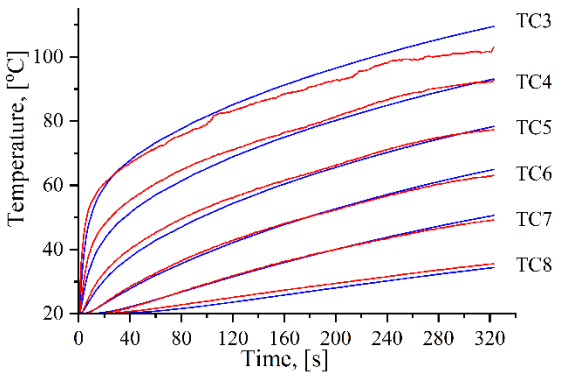

a) $f(q)$ = 5.14 °C, q = 5.70 W/mm^2.

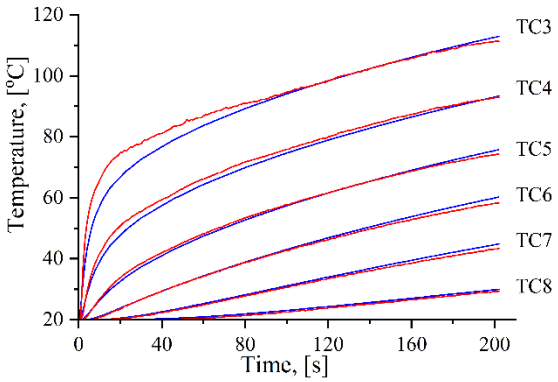

b) $f(q)$ = 5.32 °C, q = 5.24 W/mm^2.

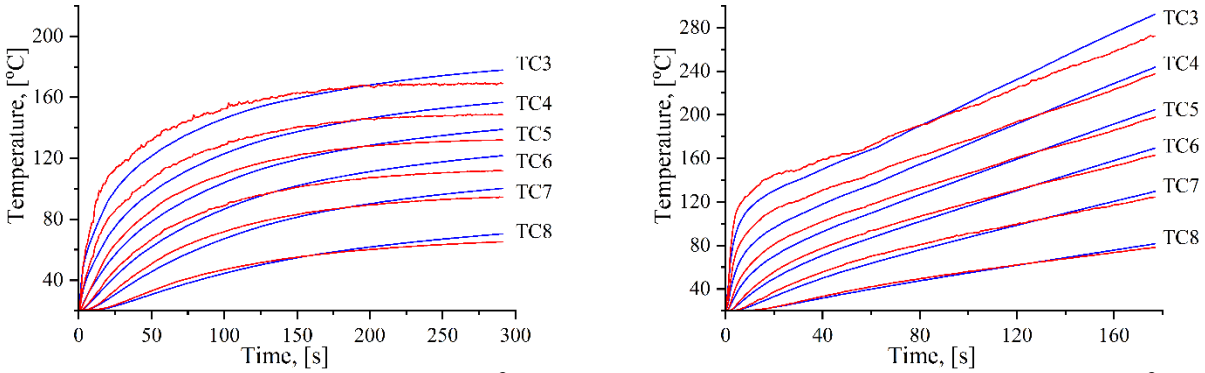

c) $f(q)$ = 27.48 °C, q = 44.27 W/mm^2. d) $f(q)$ = 33.49 °C, q = 41.14 W/mm^2.

Fig. 29. Results of the first stage: a) HSS1, b) HSS2, c) CC1, and d) CC2. Measured temperatures are red lines, calculated are blue.

As can be seen in Fig. 29, the values of the calculated temperatures and those measured for remote thermocouples practically coincide. There is a significant underestimation of the measured temperatures for TC3 and TC4. This discrepancy can be illustrated using residuals between the calculated and the measured results (Fig. 30).

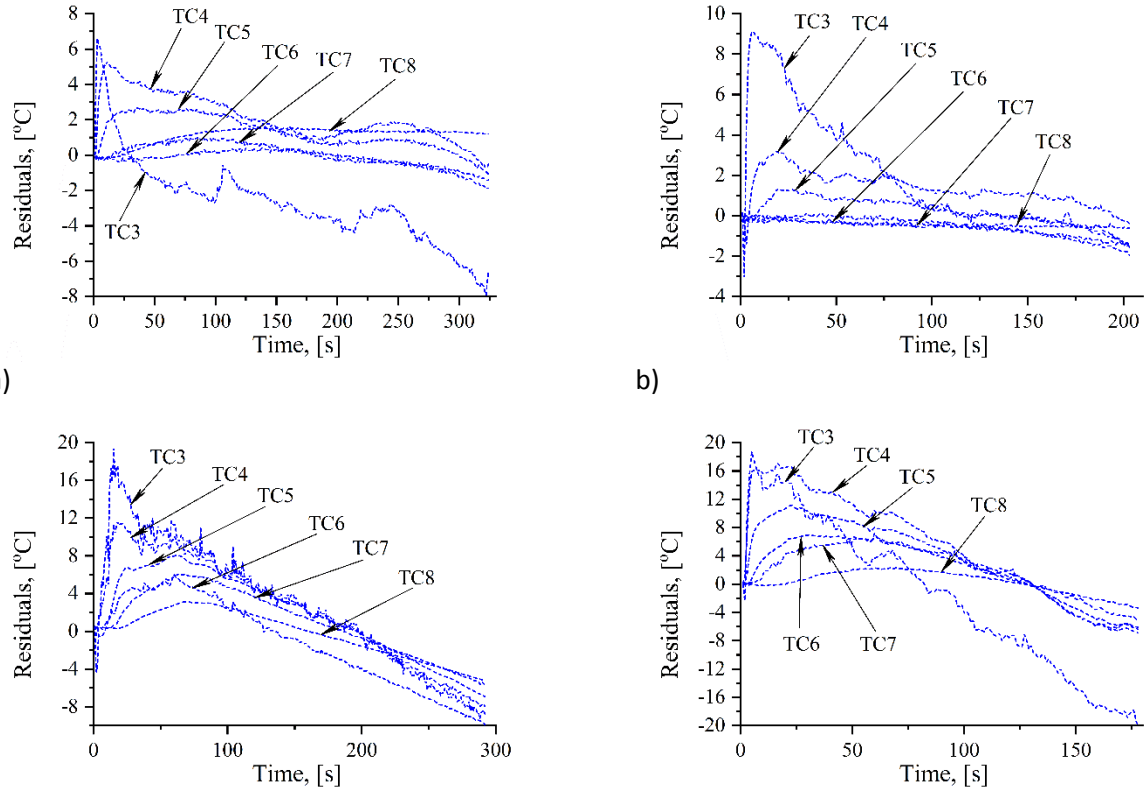

a) b)

c) d)

Fig. 30. Signed residuals between measured temperatures and calculated for assumed constant heat flux: a) HSS1, b) HSS2, c) CC1, and d) CC2.

As can be seen, Fig. 30 correspond to Fig. 27a. This shows that the L-shaped heat flux decreasing over machining time matches the data better.

Another refinement of the model can be made at this stage. As mentioned in the sensitivity analysis, the heat transfer coefficient to the environment, h, significantly affects the temperatures at all the control points and therefore needs to be refined. Initially its value was assumed to be h = 10 W/(m^{2}K) [36]. The dry machining value has been reported to be within h = 10–25 W/(m^{2}K) [15]. To identify an h value for our machining cases, the value of the heat flux q was fixed at a value (Fig. 29) and h was considered as a variable within the limits 5–25 W/(m^{2}K). The objective function graphs for these calculations are shown in Fig. 31. The minimum for the experiments HSS1 and HSS2 is reached at h = 12 W/(m^{2}K), and for the experiments CC1 and CC2 it was h = 14 W/(m^{2}K).

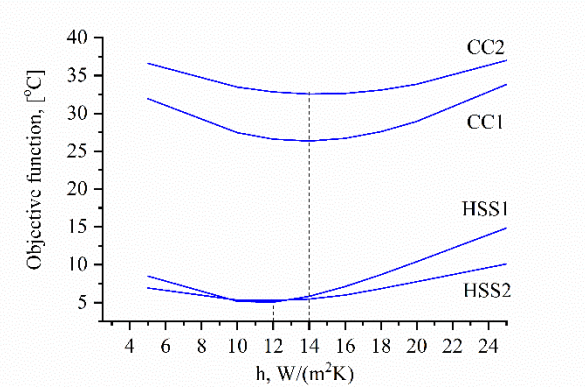

Fig. 31. Calculation results of the actual value of the heat exchange coefficient h.

The conclusion that can be drawn from this first stage emphasizes that the decreasing heat flux (L-shaped) better describes the experimental data.

3.6.2. Second stage.

Now the objective function for the decreasing flux (Fig. 26) described by Eq. 9 becomes dependent on two variables x_1, x_2 and has the form:

$$f(x\ ,x_2) = \left\|g^{calc}(t,x\ ,x_2) - g^{meas}(t)\right\| = \frac{1}{\sqrt{T}}\sqrt{\int_0^T \left(\sum_{i=1}^{n} u_i^{calc}(t,x\ ,x_2) - u_i^{meas}(t)\right)^2 dt} \to min, \qquad (12)$$

The following constraints complete the optimization problem:

$$0 \le x_2 < x\ \le \frac{P}{bA}. \qquad (13)$$

It should be noted that in the second stage, the inverse problem is again reduced to the well-posed parameter estimation problem. With the help of the penalty function technique [35], the problem (12)–(13) can be transformed to unconstrained optimization and solved by the derivative-free Nelder-Mead method [37]. The effectiveness of this method depends on the choice of the starting point (x_1^0, x_2^0). In our case, the parameter (x_1^0, x_2^0) must be chosen in such a way that the total amount of energy coming to the tool is close to that obtained at the first stage. The calculation results of the second stage are shown in Fig. 32.

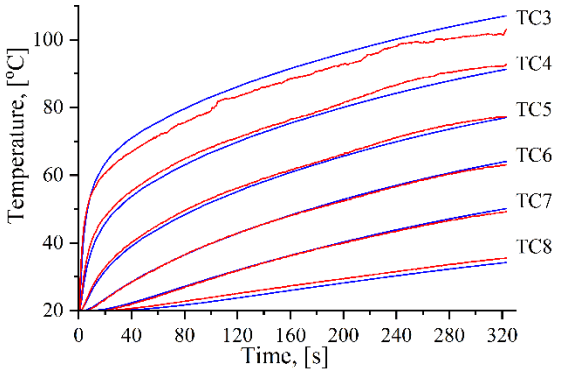

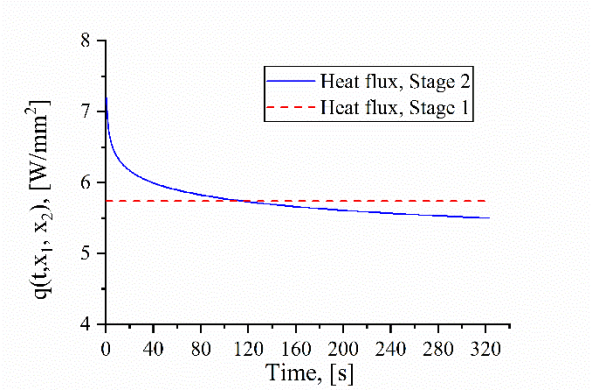

a) *f(q)* = 1.48 °C.

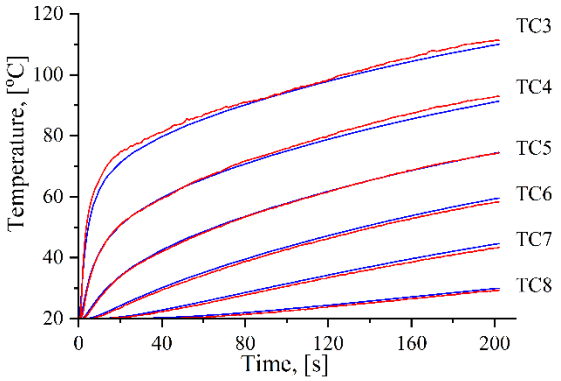

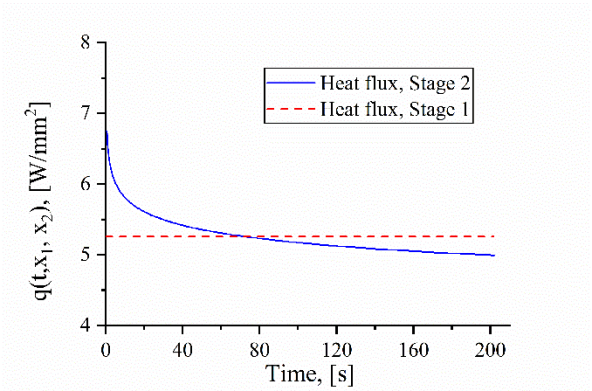

b) *f(q)* = 1.23 °C.

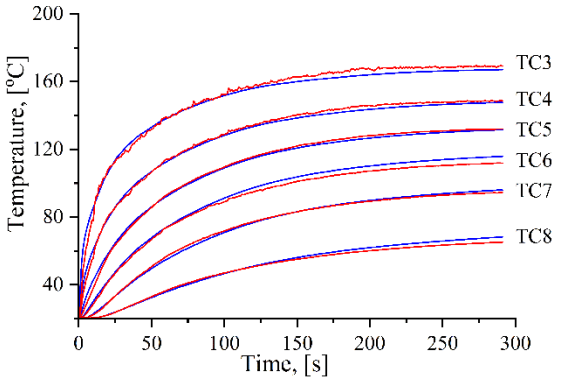

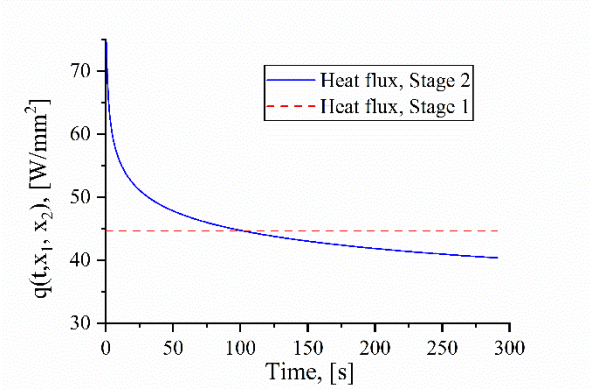

c) *f(q)* = 4.57 °C.

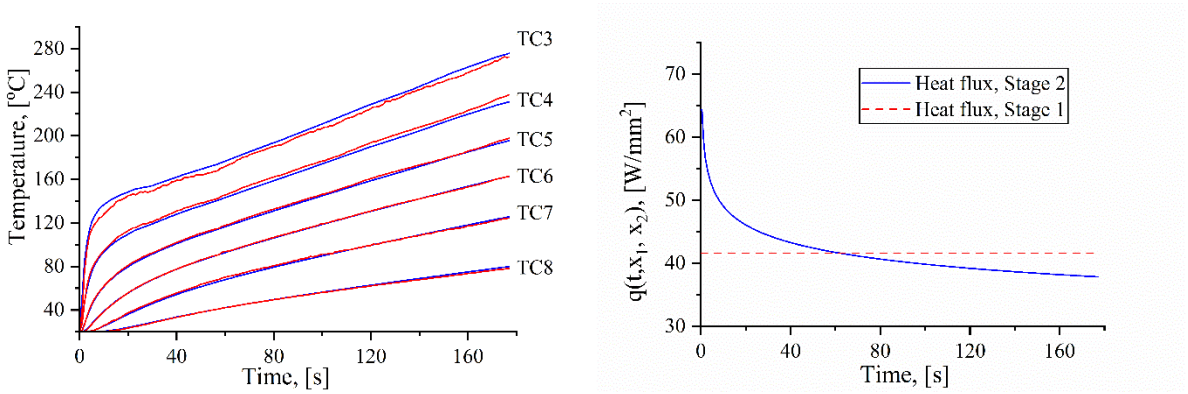

d) $f(q)$ = 3.20 °C.

Fig. 32. Measured (red) vs. calculated (blue) temperatures with respective objective functions and retrieved heat fluxes for (a) HSS1, (b) HSS2, (c) CC1, and (d) CC2 cases.

When comparing the fluxes obtained in the first and second stages, the specific tool heating energy E_t (Eq. 10) was found to be instrumental.

Table 3

Comparison of specific tool heating energy E_t.

Experiment	Specific tool heating energy E_t, J/mm^2	
	Stage 1	Stage 2
HSS1	1842.1	1852.5
HSS2	1058.8	1061.8
CC1	12881.6	13000
CC2	7281.8	7364.1

Comparison of the data in Table 3 shows that the specific tool heating energy is practically identical for both calculation stages. This means that the first stage returns an equivalent heat flux in the sense of the specific tool heating energy E_t. Then, the second stage redistributes this energy via heat flux time dependency to converge the measured and calculated temperatures.

The fraction of the total cutting power consumed by the tool body, that is, the heat partition coefficient β, can by assessed using E_t (Table 4).

Table 4

Summary of process energy consumption parameters.

Experiment	Average force F_c, N	Geometry of tool-chip interface		Cutting speed, m/min	Total power, W	Power consumed by the tool, W	Heat partition coefficient β, %
		b, mm	A, mm				
HSS1	382.73	4.15	0.86	300	1913.64	20.35	1.06
HSS2	527.65	4.55	1.03	300	2638.25	24.56	0.93
CC1	756.90	4.37	0.47	100	1261.50	90.68	7.19

CC2	1353.45	4	1	100	2255.75	164.56	7.30

3.7. On modeling an alternative behavior of heat flux time dependency

The proposed second stage approach makes it possible to analyze alternatives for simulating the heat flux behavior over time. To do this, two computational experiments were carried out.

Computational experiment 1. Assume that the heat flux behaves as shown in Fig. 33. As mentioned before, the heat flux behavior was found in [14, 15].

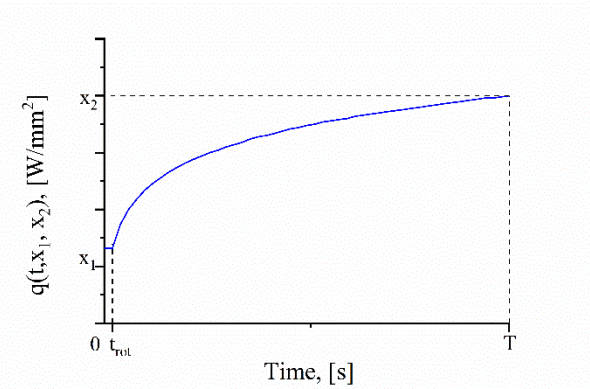

Fig. 33. The parametrized piecewise curve to describe the Γ-shaped behavior of the heat flux.

For this curve, it is also convenient to use a parameterized piecewise function (Eq. 9) but with positive power *p*. Then the optimization problem analogous to stage 2 was solved with the restriction on the values of the parameters in the form:

$$0 \le x \ < x_2 \le \frac{P}{bA}. \tag{14}$$

The values of the objective function for all three hypotheses of flux behavior and all experiments are summarized in . It can be seen that the decreasing (L-shaped) flux behavior in the form of a curve described by Eq. 9 returns the best convergence of measured and calculated temperatures. This proofs that the decreasing behavioral trend is the most adequate among the three tested hypotheses.

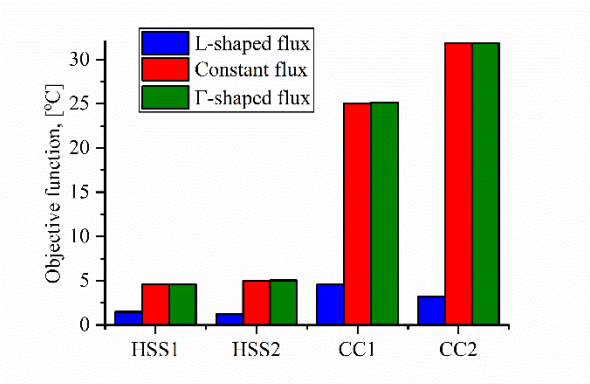

Fig. 34. Comparison of the three hypotheses.

It should be noted that the optimization routine degenerates the Γ-shaped increasing flux practically into a constant flux (Fig. 35). Restrictions (Eq. 14) on the curve parameters prevent its transformation into the L-shaped heat flux.

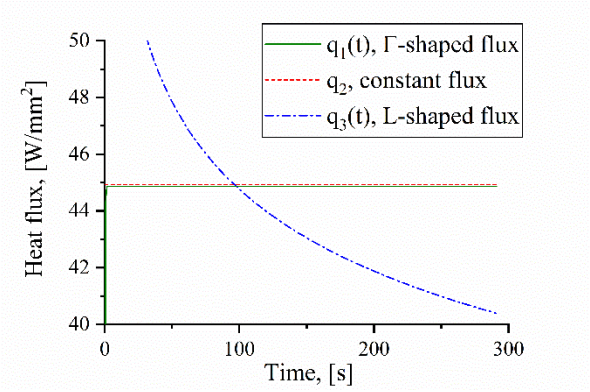

Fig. 35. The heat fluxes after second stage optimization for CC1 case.

Computational experiment 2. This experiment concerns the choice of L-shaped curve and answers the question whether other suitable L-shaped curves are applicable. Let us analyze the following decreasing curves (Fig. 36a) using different parametrization:

1. Piecewise L-shaped curve (Eq. 9) considered here for comparison,
2. $y = B(t - c)^p$,
3. $y = \frac{Bt}{c+t}$,
4. $y = y_0 + A_1 \exp\left(-\frac{t}{t_1}\right)$,
5. $y = \frac{A_1 - A_2}{1+\exp\left(\frac{x-x_0}{d}\right)} + A_2$,
6. $y = \frac{A_1 - A_2}{1+\left(\frac{x}{x_0}\right)^p} + A_2$,

where B, p, c, A_1, A_2, x_0, y_0 t_1, d are the sought parameters.

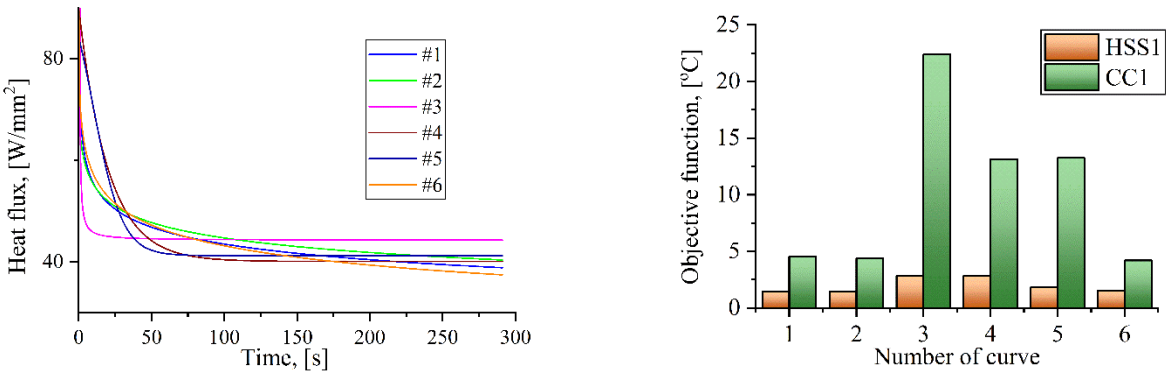

a) b)

Fig. 36. (a) Selected set of curves with equivalent energy E_t, and (b) comparison results.

Each curve was tested on the second stage for experimental cases CC1 and HSS1. The initial values of the curve parameters were chosen to provide identical specific tool heating energy E_t found in stage one (Fig. 29).

The comparisons are shown in Fig. 36b. The best objective function value is for curve number 6 in the CC1 case, with a slight advantage over curve 1. In the HSS1, case curve number 1 used in section 3.6.2 was the winner. Even though curve 6 ensures the highest accuracy in the CC1 case, it has four parameters, which dramatically increases the computational effort. Therefore, a two-parameter L-shaped curve (Eq. 9) is a reasonable compromise between the fitting accuracy and the computational effort. It is worth mentioning that this second computational experiment answers which of the six tested curves describes the decreasing flux more accurately, but the question, which is the physically correct behavior, remains open.

Conclusions

This study builds a proof of the time dependency of the heat flux that is transferred into a tool body. Due to the practical impossibility of measuring flux directly, an approach based on the inverse heat conduction technique was used. A special experimental setup was designed and manufactured to minimize temperature measurement inaccuracy because this approach is very sensitive to measurement errors. A two-stage procedure was developed to overcome the ill-posedness of the inverse heat conduction problem. This two-stage procedure transforms the ill-posed function estimation problem into a well-posed parameter estimation inverse problem. The first stage retrieves the value of the heat flux (constant over time) and specific tool heating energy E_t. The role of the second stage is to redistribute found amount of energy over time by parametrizing and comparing predefined heat flux behaviors. Solution of the second stage for machining with cemented carbide and high speed steel tooling proved that the time dependency of the heat flux is best described by a decreasing power function. Additionally, the developed method has its own value because it reliably measures energy consumption parameters of the cutting process.

As of now, reconstruction of a temperature field in a cutting tool via inverse problem techniques has not found industrial implementation because it lacks reliability due to missing knowledge regarding heat flux and its time-dependency, spatial distribution of the flux over tool-chip interface, heat exchange with environment, etc. Current findings on the decreasing behavior of the flux resolves the issue of time-dependency and make temperature reconstruction easier to address. However, the question of the exact shape of the decreasing trend, which is currently approximated by a power function, remains open. Similarly, the questions how the conditions of the machining process are governing the flux functional behavior and how it reflects the thermal phenomena in the cutting zone are also open.

References

[1] J.-E. Stahl, Metal Cutting: Theories and Models. Fagersta, SECO Tools, 2012.

[2] L. Chen, B.L. Tai, R.G. Chaudhari, X. Song, A.J. Shih, Machined surface temperature in hard turning, Int. J. of Machine Tools & Manufacture 121 (2017) 10–21.

[3] A.O. Tay, M.G. Stevenson, G. DeVahl Davis, P.L.B. Oxley, A numerical method for calculating temperature distributions in machining, from force and shear angle measurements, Int. J. Mach. Tool Des. Res. 16 (1976) 335–349.

[4] O. M. Alifanov, Inverse Heat Transfer Problems, Springer, 1994.

[5] J.V. Beck, B. Blackwell, Ch.R.St. Clair Jr., Inverse Heat Conduction: Ill-Posed Problems, New-York, Wiley-Interscience, 1985.

[6] K. Woodbury, Inverse Engineering Handbook, CRC Press, Boca Raton, 2002.

[7] H.R.B. Orlande, O.Fudym, D.Maillet, R.M.Cotta, Thermal Measurements and Inverse Techniques, CRC Press, Taylor & Francis Group, 2011

[8] V.A. Morozov, M. Stessin, Regularization Methods for Ill-Posed Problems, CRC Press, Boca Raton, 1992.

[9] A. N. Tikhonov, V. Y. Arsenin, Solution of Ill-posed Problems, Washington, Winston & Sons, 1977.

[10] J.-L. Battaglia, J.-C. Batsale, Estimation of heat flux and temperature in a tool during turning, Inverse Prob Eng 8 (2000) 435–456.

[11] J.-L. Battaglia, A. Kusiak, Estimation of heat fluxes during high-speed drilling, Int J Adv Manuf Technol 26 (2005) 750–758.

[12] J.-L. Battaglia, Multiple heat fluxes estimation using the noninteger system identification approach: application on the milling process, Inverse Probl Sci Eng, 13 (2005) 1–22.

[13] V. Norouzifard, M. Hamedi, A three-dimensional heat conduction inverse procedure to investigate tool–chip thermal interaction in machining process, Int J Adv Manuf Technol 74 (2014) 1637–1648.

[14] V. Norouzifard, M. Hamedi, Experimental determination of the tool–chip thermal contact conductance in machining process, Int. J. of Machine Tools & Manufacture 84 (2014) 45–57.

[15] R.F. Brito, S.R. Carvalho, S.M.M. Lima E Silva, Experimental investigation of thermal aspects in a cutting tool using COMSOL and inverse problem, Appl Therm Eng 86 (2015) 60–68.

[16] Ch.-H. Huang, Li-Chun Jan, R. Li, A.J. Shih, A three-dimensional inverse problem in estimating the applied heat flux of a titanium drilling – Theoretical and experimental studies, Int J Heat and Mass Transfer 50 (2007) 3265–3277.

[17] M. Putz, G. Schmidt, U. Semmler, M. Dix, M. Bräunig, M. Brockmann, S. Gierlings, Heat Flux in Cutting: Importance, Simulation and Validation, Procedia CIRP 31 (2015) 334–339.

[18] J. Yvonnet, D. Umbrello, F. Chinesta, F. Micari, A simple inverse procedure to determine heat flux on the tool in orthogonal cutting, Int J Mach Tool Manu 46 (2006) 820–827.

[19] J. Artozoul, Ch. Lescalier, D. Dudzinski, Experimental and analytical combined thermal approach for local tribological understanding in metal cutting, Appl Therm Eng 89 (2015) 394-404

[20] V. Kryzhanivskyy, V. Bushlya, O. Gutnichenko, R. M'Saoubi, J.-E. Ståhl, Computational and experimental inverse problem approach for determination of time dependency of heat flux in metal cutting, Procedia CIRP 58 (2017) 122 – 127.

[21] M. A. Davies, T. Ueda, R. M'Saoubi, B. Mullany, A. L. Cooke, On the measurement of temperature in material removal processes, Annals of the CIRP Vol. 56/2/2007, pp.581 -604.

[22] G. Dour, M. Dargusch, C. Davidson, Recommendations and guidelines for the performance of accurate heat transfer measurements in rapid forming processes, Int J Heat and Mass Transfer 49 (2006) 1773–1789.

[23] M. H. Attia, L. Kops, A new approach to cutting temperature prediction considering the thermal constriction phenomenon in multi-layer coated tools, CIRP Annals – Manu Tech 53 (2004) 47–52.

[24] http://www.uddeholm.com/files/PB_Uddeholm_vanadis_23_english.pdf, accessed March 2018.

[25] E. M. Trent, P. K. Wright, Metal Cutting, Butterworth-Heinemann, 2000.

[26] V. A. Ostafiev, Fundamentals of Physics of Metal Cutting, Kyiv, Vyscha shkola, 1976.

[27] V. Kryzhanivskyy, V. Bushlya, O. Gutnichenko, R. M'Saoubi, J.E. Ståhl, Influence of Tool Material and Tool Wear on Tool Temperature in Hard Turning Reconstructed via Inverse Problem Solution, Journal of Superhard Materials 39 (2017) 192–202.

[28] https://www.omega.com/techref/colorcodes.html, accessed March 2018.

[29] A. Bejan, A.D. Kraus, Heat Transfer Handbook, John Wiley & Sons, 2003.

[30] S. Sawada, R. Ando, S. Nomura, Thermal expansion and specific heat of tungsten oxide at high temperatures, Physical Review 84 (1951) 1054-1055.

[31] H. Wang, Y. Xu, M. Goto, Y. Tanaka, M. Yamazaki, A. Kasahara, M. Tosa, Thermal conductivity measurement of tungsten oxide nanoscale thin films, Materials Transactions 47 (2006) 1894-1897.

[32] https://www.omega.co.uk/pptst/OB_BOND_CHEM_SET.html, accessed July 2018.

[33] A.N.Kolmogorov, S.V.Fomin, Elements of the Theory of Functions and Functional Analysis, New York, Graylock Press, 1999.

[34] J. Jost, Partial Differential Equations, New York, Springer, 2002.

[35] J. F. Shapiro, Mathematical Programming: Structures and Algorithms, New York, Wiley-Interscience, 1979.

[36] V. Kryzhanivskyy, V. Bushlya, O. Gutnichenko, I.A. Petrusha, J.-E. Ståhl, Modelling and Experimental Investigation of Cutting Temperature when Rough Turning Hardened Tool Steel with PCBN Tools, Procedia CIRP 31 (2015) 489 – 495.

[37] A. Mordecai, Nonlinear Programming: Analysis and Methods, Dover Publishing, 2003.

Acknowledgments

This paper was co-funded by the European Union's Horizon 2020 Research and Innovation Programme under the Flintstone2020 project (grant agreement No 689279). It was also co-funded by the research project Sustainable Production Initiative (SPI) involving cooperation between Lund University and Chalmers University of Technology. One of the authors (VK) wishes to acknowledge VINNMER grant (2016-02046). The authors would also like to acknowledge Dr. Malin Mårtensson (Sandvik Mining and Rock Technology AB) for the supply of solid cemented carbide blocks and Mikael Hörndahl (Lund University) for help with the manufacture of tooling.